

Lattice Boltzmann model capable of mesoscopic vorticity computation

Cheng Peng

Department of Mechanical Engineering, University of Delaware, Newark, Delaware 19716-3140, USA

Zhaoli Guo

State Key Laboratory of Coal Combustion, Huazhong University of Science and Technology, Wuhan, People's Republic of China

Lian-Ping Wang

Department of Mechanical Engineering, University of Delaware, Newark, Delaware 19716-3140, USA

and State Key Laboratory of Coal Combustion, Huazhong University of Science and Technology, Wuhan, People's Republic of China

(Received 21 September 2016; revised manuscript received 3 August 2017; published 6 November 2017)

It is well known that standard lattice Boltzmann (LB) models allow the strain-rate components to be computed mesoscopically (i.e., through the local particle distributions) and as such possess a second-order accuracy in strain rate. This is one of the appealing features of the lattice Boltzmann method (LBM) which is of only second-order accuracy in hydrodynamic velocity itself. However, no known LB model can provide the same quality for vorticity and pressure gradients. In this paper, we design a multiple-relaxation time LB model on a three-dimensional 27-discrete-velocity (D3Q27) lattice. A detailed Chapman-Enskog analysis is presented to illustrate all the necessary constraints in reproducing the isothermal Navier-Stokes equations. The remaining degrees of freedom are carefully analyzed to derive a model that accommodates mesoscopic computation of all the velocity and pressure gradients from the nonequilibrium moments. This way of vorticity calculation naturally ensures a second-order accuracy, which is also proven through an asymptotic analysis. We thus show, with enough degrees of freedom and appropriate modifications, the mesoscopic vorticity computation can be achieved in LBM. The resulting model is then validated in simulations of a three-dimensional decaying Taylor-Green flow, a lid-driven cavity flow, and a uniform flow passing a fixed sphere. Furthermore, it is shown that the mesoscopic vorticity computation can be realized even with single relaxation parameter.

DOI: [10.1103/PhysRevE.96.053304](https://doi.org/10.1103/PhysRevE.96.053304)

I. INTRODUCTION

As a viable numerical method for computational fluid dynamics (CFD), the lattice Boltzmann method (LBM) is gaining its popularity because of its easiness in programming, flexibility in treating solid boundary and fluid-fluid interfaces, and excellent scalability in parallel computation [1,2]. Well known for its second-order accuracy in space and time, the standard LBM is usually compared with the second-order finite-difference (FD) or finite-volume (FV) schemes based on solving the Navier-Stokes equations. In many occasions, LBM is observed to have better performance than these conventional FD or FV schemes in terms of both accuracy and robustness. For example, Dellar [3] showed that LBM coupled with large bulk viscosity was free of spurious vortices that had been observed in the FD schemes for two-dimensional (2D) double-shear flow [4]. Gao *et al.* [5] found that the dissipation rate in a decaying homogeneous isotropic turbulence obtained with LBM was much more accurate than that from the second-order FD scheme [6], when compared with the same benchmark from the pseudospectral (PS) method. The high fidelity of LBM can be attributed to at least three origins. First, the advection term in the Boltzmann equation is treated exactly in LBM by a Lagrangian streaming process, implying that the advection term in the resulting Navier-Stokes (N-S) equations according to the Chapman-Enskog analysis is of low numerical dissipation. On the other hand, in conventional second-order FD or FV, the intrinsic truncation errors of spatial discretization always introduce artificial dispersion and dissipation to the flow [7]. Second, the collision model in LBM preserves the exact local mass and momentum conservation, which may

or may not be achieved by FD or FV schemes. Third, the strain-rate tensor in LBM can be mesoscopically obtained from the nonequilibrium distributions. This feature offers the second-order accuracy in strain-rate calculation in LBM [8–10], whereas, for the second-order FD or FV schemes, the resulting strain-rate components usually have the first-order accuracy only.

By design, the particle distribution functions in LBM contain both the equilibrium part and the nonequilibrium part. In most cases, the equilibrium part is related to the conserved moments, namely density (or pressure) and fluid hydrodynamic momentum, while the nonequilibrium part is related to the strain-rate components [11]. Together, they can satisfy the N-S equations. The usual design process does not involve vorticity, and no existing LBM can allow vorticity to be computed in terms of the local nonequilibrium distributions. Therefore, the vorticity calculation in LBM generally relies on FD approximations of velocity gradients [12], which degrades the order of accuracy for vorticity to the first order. As the most intuitive (not necessarily accurate) representation of vortical structures, accurate vorticity calculation is of great importance in many fluid mechanics problems, especially in turbulent flows. It must be noted that vorticity is a local flow property, whereas vortical structures represent a coherent distribution of vorticity over a finite region in space [13]. Better ways of identifying vortical structures may require a more complete knowledge of velocity gradient tensor [14–16]. Clearly, a direct, mesoscopic computation of vorticity from distribution functions in LBM is desired for several reasons. First, mesoscopic computation of hydrodynamic quantities in

LBM only relies on the local information. In large-scale computations with multiple processors, such local computation needs no data communications between processors and is free of any adverse effect associated with the boundary geometric complexity. Second and more importantly, since the LBM has the second-order accuracy in its distribution functions, the vorticity obtained directly and locally from the distribution functions, if possible, is expected to share the same order of accuracy.

In the past, this desire is usually unfulfilled due to the widely accepted facts that the lattice grids and the associated equilibrium distribution functions, based on which LBM is developed, are designed to maximize the isotropy at all orders [17]. Under this consideration, the resulting higher-order moments of the distribution did not provide direct links to the local flow vorticity which represents the antisymmetric property of the local velocity gradient tensor. It is important to realize that the hydrodynamic constraints required by the N-S equations represent only a subset of the moment equations [18,19], namely the number of the degrees of freedom in the distribution function in a LBM model is usually much larger than the number of hydrodynamic constraints.

The question we ask in this paper is whether those degrees of freedom not used in the N-S equations can be utilized to allow mesoscopic vorticity computation. We shall explore the possibility of redesigning LBM for this purpose. A multiple-relaxation time (MRT) LBM on a three-dimensional 27-velocity (D3Q27) lattice grid is chosen, mainly based on two considerations. First, compared with the single-relaxation time (SRT) counterparts, the MRT LBM usually has a better flexibility in relaxing the different physically irrelevant moments and in configuring their equilibrium distributions [17,20,21]. Furthermore, a mesoscopic forcing term can introduce additional flexibility [19]. Second, the D3Q27 lattice possesses adequate degrees of freedom than those base on other popular 3D lattices with smaller amounts of discrete particle velocities, e.g., D3Q15 and D3Q19. Since the D3Q27 lattice actually contains all the particle velocities in D3Q15 and D3Q19, we might argue that if a certain property is not contained in D3Q27, then it is very unlikely that such property can be found in D3Q19 or D3Q15.

The rest of the paper is arranged as follows. In Sec. II, a detailed *bottom-up* inverse design based on the Chapman-Enskog analysis is presented. By the inverse design, we view the isothermal N-S equations as our design goal and construct the mesoscopic model details based on the hydrodynamic constraints. This process offers a clear picture on the minimum set of constraints a mesoscopic LBM model must satisfy in order to remain consistent with the hydrodynamic equations. At the same time, it will reveal the maximum unconstrained degrees of freedom that could potentially be used to configure the mesoscopic vorticity calculation. A systematic discussion of how these remaining degrees of freedom can be feasibly used to fulfill the mesoscopic vorticity calculation is offered in Sec. III. An asymptotic analysis is also provided to prove the second-order accuracy of the mesoscopic vorticity calculation. In Sec. IV, the proposed model is validated via three benchmark tests, a three-dimensional (3D) Taylor-Green vortex flow, a 3D lid-driven cavity flow, and a 3D uniform stream passing a fixed sphere. Both qualitative and quantitative observations

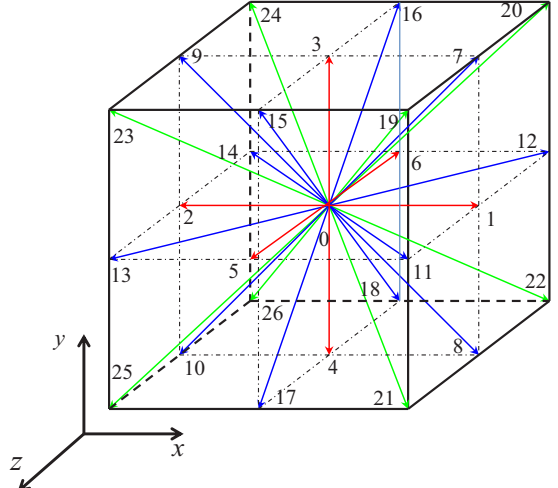


FIG. 1. Sketch of D3Q27 lattice grid.

are made regarding the reliability and accuracy of the proposed mesoscopic vorticity calculation. The main conclusions of the current study are recapitulated in Sec. V. At last, a *top-down* analysis in terms of the equilibrium distribution is given in the Appendix to offer an alternative explanation of the key idea in our model design. This top-down explanation is based on the results from the bottom-up derivation.

II. AN INVERSE DESIGN OF D3Q27 MRT MODEL

A. Construction of moments and transform matrix

A D3Q27 lattice grid is shown in Fig. 1. Its 27 discrete particle velocities can be expressed as

$$\mathbf{e}_\alpha = \begin{cases} (0,0,0)c & \alpha = 0, \\ (\pm 1,0,0)c & \alpha = 1,2, \\ (0,\pm 1,0)c & \alpha = 3,4, \\ (0,0,\pm 1)c & \alpha = 5,6, \\ (\pm 1,\pm 1,0)c & \alpha = 7-10, \\ (\pm 1,0,\pm 1)c & \alpha = 11-14, \\ (0,\pm 1,\pm 1)c & \alpha = 15-18, \\ (\pm 1,\pm 1,\pm 1)c & \alpha = 19-26. \end{cases} \quad (1)$$

A set of 27 distributions, written in vector form as \mathbf{f} , is associated with these 27 discrete particle velocities. The same number of independent moments, denoted by \mathbf{m} , can be defined through linear transformation of the distribution functions. When constructing the moments, we always proceed with increasing order, from the zeroth-order, to the first-order, and then the second-order moments, and so on. All independent moments at a given order are exhausted first before proceeding to the next order. A Gram-Schmidt procedure [22], i.e.,

$$\mathbf{M}_j = \tilde{\mathbf{M}}_j - \sum_{i=0}^{j-1} \frac{\tilde{\mathbf{M}}_j \cdot \mathbf{M}_i}{\mathbf{M}_i \cdot \mathbf{M}_i} \mathbf{M}_i, \quad (j \geq 1), \quad (2)$$

is applied to the row vectors $\tilde{\mathbf{M}}_j$ of the raw transform matrix $\tilde{\mathbf{M}}$ to ensure orthogonality between any two row vectors in the finalized transform matrix \mathbf{M} . This procedure results in a

finalized orthogonal transform matrix \mathbf{M} that reads

and 27 independent and orthogonal moments, which are summarized as:

- (i) the zeroth-order moment (1)

$$m_0 = \sum_{\alpha} f_{\alpha},$$

- (ii) the first-order moments (3)

$$m_1 = \sum_{\alpha} f_{\alpha} e_{\alpha x}, \quad m_2 = \sum_{\alpha} f_{\alpha} e_{\alpha y}, \quad m_3 = \sum_{\alpha} f_{\alpha} e_{\alpha z},$$

- (iii) the second-order moments (6)

$$m_4 = \sum_{\alpha} f_{\alpha} (\|\mathbf{e}_{\alpha}\|^2 - 2), \quad m_5 = \sum_{\alpha} f_{\alpha} (3e_{\alpha x}^2 - \|\mathbf{e}_{\alpha}\|^2), \quad m_6 = p_{zz} = \sum_{\alpha} f_{\alpha} (e_{\alpha y}^2 - e_{\alpha z}^2),$$

$$m_7 = \sum_{\alpha} f_{\alpha} e_{\alpha x} e_{\alpha y}, \quad m_8 = \sum_{\alpha} f_{\alpha} e_{\alpha y} e_{\alpha z}, \quad m_9 = \sum_{\alpha} f_{\alpha} e_{\alpha x} e_{\alpha z},$$

- (iv) the third-order moments (7)

$$\begin{aligned} m_{10} &= \sum_{\alpha} f_{\alpha}(3\|\mathbf{e}_{\alpha}\|^2 - 7)e_{\alpha x}, \quad m_{11} = \sum_{\alpha} f_{\alpha}(3\|\mathbf{e}_{\alpha}\|^2 - 7)e_{\alpha y}, \quad m_{12} = \sum_{\alpha} f_{\alpha}(3\|\mathbf{e}_{\alpha}\|^2 - 7)e_{\alpha z}, \\ m_{13} &= \sum_{\alpha} f_{\alpha}(e_{\alpha y}^2 - e_{\alpha z}^2)e_{\alpha x}, \quad m_{14} = \sum_{\alpha} f_{\alpha}(e_{\alpha z}^2 - e_{\alpha x}^2)e_{\alpha y}, \quad m_{15} = \sum_{\alpha} f_{\alpha}(e_{\alpha x}^2 - e_{\alpha y}^2)e_{\alpha z}, \\ m_{16} &= \sum_{\alpha} f_{\alpha}e_{\alpha x}e_{\alpha y}e_{\alpha z}, \end{aligned}$$

(v) the fourth-order moments (6)

$$m_{17} = \sum_{\alpha} f_{\alpha} (3\|\mathbf{e}_{\alpha}\|^4 - 11\|\mathbf{e}_{\alpha}\|^2 + 8), \quad m_{18} = \sum_{\alpha} f_{\alpha} (3\|\mathbf{e}_{\alpha}\|^2 - 5)(3e_{\alpha x}^2 - \|\mathbf{e}_{\alpha}\|^2), \quad m_{19} = \sum_{\alpha} f_{\alpha} (3\|\mathbf{e}_{\alpha}\|^2 - 5)(e_{\alpha y}^2 - e_{\alpha z}^2),$$

$$m_{20} = \sum_{\alpha} f_{\alpha} (3\|\mathbf{e}_{\alpha}\|^2 - 8)e_{\alpha x}e_{\alpha y}, \quad m_{21} = \sum_{\alpha} f_{\alpha} (3\|\mathbf{e}_{\alpha}\|^2 - 8)e_{\alpha y}e_{\alpha z}, \quad m_{22} = \sum_{\alpha} f_{\alpha} (3\|\mathbf{e}_{\alpha}\|^2 - 8)e_{\alpha x}e_{\alpha z},$$

(vi) the fifth-order moments (3)

$$m_{23} = \sum_{\alpha} f_{\alpha} \left(\frac{9}{2}\|\mathbf{e}_{\alpha}\|^4 - \frac{39}{2}\|\mathbf{e}_{\alpha}\|^2 + 19 \right) e_{\alpha x}, \quad m_{24} = \sum_{\alpha} f_{\alpha} \left(\frac{9}{2}\|\mathbf{e}_{\alpha}\|^4 - \frac{39}{2}\|\mathbf{e}_{\alpha}\|^2 + 19 \right) e_{\alpha y},$$

$$m_{25} = \sum_{\alpha} f_{\alpha} \left(\frac{9}{2}\|\mathbf{e}_{\alpha}\|^4 - \frac{39}{2}\|\mathbf{e}_{\alpha}\|^2 + 19 \right) e_{\alpha z},$$

(vii) the sixth order moment (1)

$$m_{26} = \sum_{\alpha} f_{\alpha} \left(\frac{9}{2}\|\mathbf{e}_{\alpha}\|^6 - \frac{45}{2}\|\mathbf{e}_{\alpha}\|^4 + 30\|\mathbf{e}_{\alpha}\|^2 - 8 \right).$$

B. Inverse design of a D3Q27 MRT model

The idea of the inverse design is to use the N-S equations as design constraints to help determine the minimum number of equilibrium moments. By doing so, we maximize the flexibility of our model that could be potentially used for the mesoscopic vorticity calculation. In this work, we follow the same inverse design procedure as presented in Refs. [10,21,23]. All the equilibrium moments $m_{\alpha}^{(\text{eq})}$ are unspecified at the beginning. Some of them will be determined later via the Chapman-Enskog (C-E) analysis. Unlike the standard multi-scale expansion in C-E analysis that is performed in terms of the distribution functions, the C-E analysis shown below is done in the moment space. This alteration does not change the nature of the C-E expansion but is easier to derive the governing equations for all moments. Same as in the other MRT LB models, the evolution equation is

$$\mathbf{f}(\mathbf{x} + \mathbf{e}_{\alpha}\delta_t, t + \delta_t) - \mathbf{f}(\mathbf{x}, t) = -\mathbf{M}^{-1}\mathbf{S}[\mathbf{m}(\mathbf{x}, t) - \mathbf{m}^{(\text{eq})}(\mathbf{x}, t)]. \quad (4)$$

where \mathbf{m} is the moment vector and $\mathbf{m}^{(\text{eq})}$ is the corresponding equilibrium-moment vector, \mathbf{x} is the spatial location, t is the time, δ_t is the time step size, and \mathbf{S} is a diagonal matrix containing 27 relaxation parameters $\mathbf{S} = \text{diag}(s_0, s_1, \dots, s_{26})$. Multiplying the transform matrix \mathbf{M} to the above equation, and then applying the Taylor expansion to the left-hand side, the evolution equation becomes

$$(\mathbf{I}\partial_t + \hat{\mathbf{C}}_i\partial_i)\mathbf{m} + \frac{\delta_t}{2}(\mathbf{I}\partial_t + \hat{\mathbf{C}}_i\partial_i)^2\mathbf{m} = -\frac{\mathbf{S}}{\delta_t}[\mathbf{m} - \mathbf{m}^{(\text{eq})}], \quad (5)$$

where $\hat{\mathbf{C}}_i \equiv \mathbf{MC}_i\mathbf{M}^{-1}$, with \mathbf{C}_i being the diagonal matrix containing $e_{\alpha i}$. Subscript i is the spatial directions. Following the standard C-E procedure, the moments \mathbf{m} , the time, and spatial derivatives in Eq. (5) are expanded as

$$\mathbf{m} = \mathbf{m}^{(0)} + \varepsilon\mathbf{m}^{(1)} + \varepsilon^2\mathbf{m}^{(2)} + \dots, \quad (6a)$$

$$\partial_t = \varepsilon\partial_{t1} + \varepsilon^2\partial_{t2} + \dots, \quad (6b)$$

$$\partial_i = \varepsilon\partial_{1i} + \dots, \quad (6c)$$

where ε is a small number that is proportional to the Knudsen number, the ratio between the molecular mean free path to the macroscopic characteristic length. Substituting Eq. (6) into Eq. (5) and grouping all terms according to the order in ε , we obtain

$$O(1) : \mathbf{m}^{(0)} = \mathbf{m}^{(\text{eq})}, \quad (7a)$$

$$O(\varepsilon) : (\mathbf{I}\partial_{t1} + \hat{\mathbf{C}}_i\partial_{1i})\mathbf{m}^{(0)} = -\frac{\mathbf{S}}{\delta_t}\mathbf{m}^{(1)}, \quad (7b)$$

$$O(\varepsilon^2) : \mathbf{I}\partial_{t2}\mathbf{m}^{(0)} + (\mathbf{I}\partial_{t1} + \hat{\mathbf{C}}_i\partial_{1i})(\mathbf{I} - \frac{\mathbf{S}}{2})\mathbf{m}^{(1)} = -\frac{\mathbf{S}}{\delta_t}\mathbf{m}^{(2)}. \quad (7c)$$

In particular, the first four equations of Eq. (7b) can be explicitly written as

$$\partial_{t1}m_0^{(0)} + \partial_{1x}m_1^{(0)} + \partial_{1y}m_2^{(0)} + \partial_{1z}m_3^{(0)} = -\frac{s_0}{\delta_t}m_0^{(1)}, \quad (8a)$$

$$\partial_{t1}m_1^{(0)} + \partial_{1x}\left[\frac{2}{3}m_0^{(0)} + \frac{1}{3}m_4^{(0)} + \frac{1}{3}m_5^{(0)}\right] + \partial_{1y}m_7^{(0)} + \partial_{1z}m_9^{(0)} = -\frac{s_1}{\delta_t}m_1^{(1)}, \quad (8b)$$

$$\partial_{t1}m_2^{(0)} + \partial_{1x}m_7^{(0)} + \partial_{1y}\left[\frac{2}{3}m_0^{(0)} + \frac{1}{3}m_4^{(0)} - \frac{1}{6}m_5^{(0)} + \frac{1}{2}m_6^{(0)}\right] + \partial_{1z}m_8^{(0)} = -\frac{s_2}{\delta_t}m_2^{(1)}, \quad (8c)$$

$$\partial_{t1}m_3^{(0)} + \partial_{1x}m_9^{(0)} + \partial_{1y}m_8^{(0)} + \partial_{1z}\left[\frac{2}{3}m_0^{(0)} + \frac{1}{3}m_4^{(0)} - \frac{1}{6}m_5^{(0)} - \frac{1}{2}m_6^{(0)}\right] = -\frac{s_3}{\delta_t}m_3^{(1)}. \quad (8d)$$

which should yield the leading-order continuity equation and Euler equations, i.e.,

$$\partial_t\delta\rho + \partial_x(\rho_0u) + (\partial_y\rho_0v) + (\partial_z\rho_0w) = 0, \quad (9a)$$

$$\partial_t(\rho_0u) + \partial_x(p + \rho_0u^2) + \partial_y(\rho_0uv) + \partial_z(\rho_0uw) = 0, \quad (9b)$$

$$\partial_t(\rho_0v) + \partial_x(\rho_0uv) + \partial_y(p + \rho_0v^2) + \partial_z(\rho_0vw) = 0, \quad (9c)$$

$$\partial_t(\rho_0w) + \partial_x(\rho_0uw) + \partial_y(\rho_0vw) + \partial_z(p + \rho_0w^2) = 0. \quad (9d)$$

where u , v , and w are the velocity components in the x , y , and z directions, respectively. p is the pressure, which is related to density fluctuation $\delta\rho$ by the isothermal equation of state as $p = c_s^2\delta\rho$, and c_s is the speed of sound. Note here that we partition the density as a constant background density ρ_0 and a density fluctuation $\delta\rho$, following He and Luo [24].

Matching Eq. (9) with its corresponding equation in Eq. (8), the following equilibrium moments are uniquely determined:

$$m_0^{(0)} = \delta\rho, \quad m_1^{(0)} = \rho_0u, \quad m_2^{(0)} = \rho_0v, \quad m_3^{(0)} = \rho_0w, \quad (10a)$$

$$m_4^{(0)} = (3c_s^2 - 2)\delta\rho + \rho_0(u^2 + v^2 + w^2), \quad m_5^{(0)} = \rho_0(2u^2 - v^2 - w^2), \quad m_6^{(0)} = \rho_0(v^2 - w^2), \quad (10b)$$

$$m_7^{(0)} = \rho_0uv, \quad m_8^{(0)} = \rho_0vw, \quad m_9^{(0)} = \rho_0uw. \quad (10c)$$

In order to reproduce the isothermal Euler equations, the equilibria of all zeroth-, first-, and second-order moments must be uniquely derived. However, all third- and higher order moments are irrelevant moments at this stage. The leading-order nonequilibrium components of the zeroth- and first-order moments must also be set to zero, as required by the local conservation laws.

Next, we proceed to the $O(\varepsilon^2)$ equations. So far, it is clear that the zeroth- and first-order moments are density and momenta in the hydrodynamic equations, respectively. Since the N-S equations are macroscopic evolution equations of density and momenta, our remaining job is to connect these four mesoscopic moment equations with their corresponding hydrodynamic equations. Again, the four equations at $O(\varepsilon^2)$ can be explicitly written as

$$\partial_{t2}\delta\rho = -\frac{s_0}{\delta_t}m_0^{(2)}, \quad (11a)$$

$$\partial_{t2}(\rho_0u) + \partial_{1x}\left[\frac{1}{3}A_4 + \frac{1}{3}A_5\right] + \partial_{1y}A_7 + \partial_{1z}A_9 = \frac{s_1}{\delta_t}m_1^{(2)}, \quad (11b)$$

$$\partial_{t2}(\rho_0v) + \partial_{1x}A_7 + \partial_{1y}\left[\frac{1}{3}A_4 - \frac{1}{6}A_5 + \frac{1}{2}A_6\right] + \partial_{1z}A_8 = -\frac{s_2}{\delta_t}m_2^{(2)}, \quad (11c)$$

$$\partial_{t2}(\rho_0w) + \partial_{1x}A_9 + \partial_{1y}A_8 + \partial_{1z}\left[\frac{1}{3}A_4 - \frac{1}{6}A_5 - \frac{1}{2}A_6\right] = -\frac{s_3}{\delta_t}m_3^{(2)}. \quad (11d)$$

where $A_\alpha \equiv (1 - \frac{s_\alpha}{2})m_\alpha^{(1)}$, with no summation over α . It should be noted that terms in the N-S equations representing the Euler equations have already been reproduced by the leading-order moment equations. Hence, the above equations are only expected to match the remaining part, which is the difference between the N-S equations and the Euler equations, i.e.,

$$\partial_{t2}(\delta\rho) = 0, \quad (12a)$$

$$\partial_{t2}(\rho_0u_i) = \partial_{1j}\left[\mu(\partial_{1j}u_i + \partial_{1i}u_j) - \frac{2}{3}\mu(\partial_{1k}u_k)\delta_{ij} + \mu^V(\partial_{1k}u_k)\delta_{ij}\right], \quad (12b)$$

where the subscripts i , j , and k denote the spatial directions and μ and μ^V are the shear and bulk viscosity, respectively. Matching Eq. (11) with Eq. (12) leads to

$$A_4 = -3\mu^V(\partial_{1x}u + \partial_{1y}v + \partial_{1z}w), \quad (13a)$$

$$A_5 = -2\mu(2\partial_{1x}u - \partial_{1y}v - \partial_{1z}w), \quad (13b)$$

$$A_6 = -2\mu(\partial_{1y}v - \partial_{1z}w), \quad (13c)$$

$$A_7 = -\mu(\partial_{1y}u + \partial_{1x}v), \quad (13d)$$

$$A_8 = -\mu(\partial_{1y}w + \partial_{1z}v), \quad (13e)$$

$$A_9 = -\mu(\partial_{1z}u + \partial_{1x}w). \quad (13f)$$

The above results relate the leading-order nonequilibrium parts of the six second-order moments to stress components in the N-S equations. Alternatively, A_α can be also expressed in terms of equilibrium moments according to the C-E expansion on the order of $O(\varepsilon)$, i.e., Eq. (7b), as

$$A_4 = -\left(\frac{2-s_4}{2s_4}\right)\delta_t \left\{ \partial_{1x} \left[\frac{1}{3}\rho_0 u + \frac{1}{3}m_{10}^{(0)} - (3c_s^2 - 2)\rho_0 u \right] + \partial_{1y} \left[\frac{1}{3}\rho_0 v + \frac{1}{3}m_{11}^{(0)} - (3c_s^2 - 2)\rho_0 v \right] \right. \\ \left. + \partial_{1z} \left[\frac{1}{3}\rho_0 w + \frac{1}{3}m_{12}^{(0)} - (3c_s^2 - 2)\rho_0 w \right] \right\}, \quad (14a)$$

$$A_5 = -\left(\frac{2-s_5}{2s_5}\right)\delta_t \left\{ \partial_{1x} \left[\frac{2}{3}\rho_0 u - \frac{1}{3}m_{10}^{(0)} \right] + \partial_{1y} \left[-\frac{1}{3}\rho_0 v + \frac{1}{6}m_{11}^{(0)} - \frac{3}{2}m_{14}^{(0)} \right] + \partial_{1z} \left[-\frac{1}{3}\rho_0 w + \frac{1}{6}m_{12}^{(0)} + \frac{3}{2}m_{15}^{(0)} \right] \right\}, \quad (14b)$$

$$A_6 = -\left(\frac{2-s_6}{2s_6}\right)\delta_t \left\{ \partial_{1x} m_{13}^{(0)} + \partial_{1y} \left[\frac{1}{3}\rho_0 v - \frac{1}{6}m_{11}^{(0)} - \frac{1}{2}m_{14}^{(0)} \right] + \partial_{1z} \left[-\frac{1}{3}\rho_0 w + \frac{1}{6}m_{12}^{(0)} - \frac{1}{2}m_{15}^{(0)} \right] \right\}, \quad (14c)$$

$$A_7 = -\left(\frac{2-s_7}{2s_7}\right)\delta_t \left\{ \partial_{t1}(\rho_0 uv) + \partial_{1x} \left[\frac{2}{3}\rho_0 v + \frac{1}{6}m_{11}^{(0)} - \frac{1}{2}m_{14}^{(0)} \right] + \partial_{1y} \left[\frac{2}{3}\rho_0 u + \frac{1}{6}m_{10}^{(0)} + \frac{1}{2}m_{13}^{(0)} \right] + \partial_{1z} m_{16}^{(0)} \right\}, \quad (14d)$$

$$A_8 = -\left(\frac{2-s_8}{2s_8}\right)\delta_t \left\{ \partial_{t1}(\rho_0 vw) + \partial_{1x} m_{16}^{(0)} + \partial_{1y} \left[\frac{2}{3}\rho_0 w + \frac{1}{6}m_{12}^{(0)} - \frac{1}{2}m_{15}^{(0)} \right] + \partial_{1z} \left[\frac{2}{3}\rho_0 v + \frac{1}{6}m_{11}^{(0)} + \frac{1}{2}m_{14}^{(0)} \right] \right\}, \quad (14e)$$

$$A_9 = -\left(\frac{2-s_9}{2s_9}\right)\delta_t \left\{ \partial_{t1}(\rho_0 uw) + \partial_{1x} \left[\frac{2}{3}\rho_0 w + \frac{1}{6}m_{12}^{(0)} + \frac{1}{2}m_{15}^{(0)} \right] + \partial_{1y} m_{16}^{(0)} + \partial_{1z} \left[\frac{2}{3}\rho_0 u + \frac{1}{6}m_{10}^{(0)} - \frac{1}{2}m_{13}^{(0)} \right] \right\}, \quad (14f)$$

where all the known equilibrium moments have already been expressed in terms of the results in Eq. (10). Finally, matching Eqs. (13) and (14) equation by equation, and then term by term, we can obtain

$$m_{10}^{(0)} = -2\rho_0 u, \quad m_{11}^{(0)} = -2\rho_0 v, \quad m_{12}^{(0)} = -2\rho_0 w, \quad (15a)$$

$$m_{13}^{(0)} = 0, \quad m_{14}^{(0)} = 0, \quad m_{15}^{(0)} = 0, \quad m_{16}^{(0)} = 0, \quad (15b)$$

$$\nu^V = \left(\frac{2-s_4}{2s_4}\right)\frac{\delta_t}{3} \left(\frac{5}{3} - 3c_s^2\right), \quad \nu = \left(\frac{2-s_5}{2s_5}\right)\frac{\delta_t}{3},$$

$$s_5 = s_6 = s_7 = s_8 = s_9. \quad (15c)$$

where $\nu = \mu/\rho_0$ and $\nu^V = \mu^V/\rho_0$ are the kinematic shear and bulk viscosity, respectively. It shall be noted that the three time-derivative terms $\partial_{t1}(\rho_0 uv)$, $\partial_{t1}(\rho_0 vw)$, $\partial_{t1}(\rho_0 uw)$, are neglected, since they are of the order $O(Ma^3)$ and are usually neglected in LBM. At this stage, all the zeroth-, first-, second-, and third-order equilibrium moments have been uniquely determined by the constraints of the isothermal N-S equations. The fourth- and higher-order moments are irrelevant. The relaxation parameters of the six second-order moments, s_4 to s_9 , must also be appropriately defined in order to have correct bulk and shear viscosities.

C. Summary

From the inverse design process, we find that Eqs. (10) and (15) are the only necessary constraints in our MRT LB model. Among all 27 equilibrium moments, only the zeroth-, first-, second-, and third-order equilibrium moments must be properly specified. Since the isothermal N-S equations are of concern and the energy equation is not considered, it is unnecessary to constrain any fourth- or higher-order moments or the relaxation parameters for the third- or higher-order moments.

We note, however, in many previous designs [25–27] of the MRT-LB models, the equilibrium moments were acquired simply based on the matrix transform of standard LBGK equilibrium distribution,

$$f_\alpha^{(\text{LBGK, eq})} = w_\alpha \delta\rho + w_\alpha \rho_0 \left[\frac{e_{\alpha i} u_i}{c_s^2} + \frac{(e_{\alpha i} u_i)^2}{2c_s^4} - \frac{u_i u_i}{2c_s^2} \right], \quad (16)$$

where w_α is the weighting factor associated with each lattice velocity. This specification led to the determination for all equilibrium moments, which completely discarded the available flexibilities in designing the irrelevant high-order equilibrium moments. We emphasize that, although we must have $\mathbf{m} = \mathbf{Mf}$, the relation $\mathbf{m}^{(\text{eq})} = \mathbf{Mf}^{(\text{LBGK, eq})}$ is not required. The flexibility of designing those unconstrained higher-order equilibrium moments and relaxation parameters potentially offers a possibility to incorporate the mesoscopic vorticity calculation into the LBM. This possibility will be explored in detail in the next section. However, it must be made clear that the above statement may not be valid for those LBM models where high-order equilibrium moments are constrained otherwise, for example, by the energy equation or flow compressibility. In this paper, we confine our LBM model to the nearly incompressible and isothermal N-S equations.

III. HIGH-ORDER EQUILIBRIUM MOMENTS AND MOMENT EQUATIONS FOR VORTICITY CALCULATION

A. The construction of high-order equilibrium moments

Our inverse design in the last section clearly shows that in the D3Q27 MRT model, besides the 17 zeroth-, first-, second-, and third-order equilibrium moments that can be determined uniquely based on the hydrodynamic equations, the other 10 fourth- and higher-order equilibrium moments are irrelevant to the N-S equations and thus can be designed relatively freely. However, it should be made clear that the design of these 10 higher-order equilibrium moments is, by no means, completely

free. The main consideration is that the particle distribution functions in LBM must be near their equilibria. Therefore, we should expect the expressions of these high-order equilibrium moments to be consistent in form with the definitions of the moments. Specifically, it is reasonable to assume the following general forms:

$$\begin{aligned} m_{17}^{(\text{eq})} &= \alpha_{17}\delta\rho + \beta_{17}\rho_0(u^2 + v^2 + w^2), \\ m_{18}^{(\text{eq})} &= \beta_{18}\rho_0(2u^2 - v^2 - w^2), \\ m_{19}^{(\text{eq})} &= \beta_{19}\rho_0(v^2 - w^2), \quad m_{20}^{(\text{eq})} = \gamma_{20}\rho_0uv, \end{aligned} \quad (17\text{a})$$

$$m_{21}^{(\text{eq})} = \gamma_{21}\rho_0vw, \quad m_{22}^{(\text{eq})} = \gamma_{22}\rho_0uw, \quad (17\text{b})$$

$$m_{23}^{(\text{eq})} = \zeta_{23}\rho_0u, \quad m_{24}^{(\text{eq})} = \zeta_{24}\rho_0v, \quad m_{25}^{(\text{eq})} = \zeta_{25}\rho_0w, \quad (17\text{c})$$

$$m_{26}^{(\text{eq})} = \alpha_{26}\delta\rho + \beta_{26}\rho_0(u^2 + v^2 + w^2). \quad (17\text{d})$$

The coefficients α_{17} , β_{17} , β_{18} , β_{19} , γ_{20} , γ_{21} , γ_{22} , ζ_{23} , ζ_{24} , ζ_{25} , α_{26} , and β_{26} remain to be determined. We will show later that their values can be specifically designed to embed the vorticity components into the nonequilibrium moments. It is noted that the set of the standard LBGK equilibrium moments corresponds to a special setting of these coefficients, namely $\alpha_{17} = 2$, $\beta_{17} = -4$, $\beta_{18} = \beta_{19} = -1$, $\gamma_{20} = \gamma_{21} = \gamma_{22} = -1$, $\zeta_{23} = \zeta_{24} = \zeta_{25} = 1$, $\alpha_{26} = -1$, $\beta_{26} = 3$. The key here is to alter these values to realize the necessary anisotropy to enable the local vorticity calculation from the nonequilibrium moments.

B. Mesoscopic vorticity calculation from nonequilibrium moments

It is well known that all six components of the strain-rate tensor in LBM can be calculated mesoscopically in terms of the second-order nonequilibrium moments [9,28]. In our model, the vorticity components are expected to be obtained in the same manner. In MRT-LBM, the nonequilibrium moments, $m_\alpha^{(\text{neq})}$ is usually approximated as $\varepsilon m_\alpha^{(1)}$, which can be related to the time derivatives of themselves and the spatial derivatives of other equilibrium moments via C-E expansion on the order of ε , i.e., Eq. (7b). In the D3Q27 model, Eq. (7b) contains 27 subequations, the first 4 of which, as we have shown in the last section, lead to the continuity and Euler equations. The remaining 23 moment equations can be potentially used to evaluate nonconserved hydrodynamic quantities, such as

$$\begin{aligned} \partial_x \left[\left(\frac{\alpha_{17}}{3} + 6c_s^2 - \frac{8}{3} \right) \delta\rho + \left(\frac{\beta_{17}}{3} + \frac{2\beta_{18}}{3} + 2 \right) u^2 + \left(\frac{\beta_{17}}{3} - \frac{\beta_{18}}{3} + 2 \right) v^2 + \left(\frac{\beta_{17}}{3} - \frac{\beta_{18}}{3} + 2 \right) w^2 \right] \\ + (3 + \gamma_{20})\partial_y(uv) + (3 + \gamma_{22})\partial_z(uw) = -\frac{s_{10}}{\rho_0\delta_t}\varepsilon m_{10}^{(1)}, \end{aligned} \quad (19\text{a})$$

$$\begin{aligned} \partial_y \left[\left(\frac{\alpha_{17}}{3} + 6c_s^2 - \frac{8}{3} \right) \delta\rho + \left(\frac{\beta_{17}}{3} - \frac{\beta_{18}}{3} + 2 \right) u^2 + \left(\frac{\beta_{17}}{3} + \frac{\beta_{18}}{6} + \frac{\beta_{19}}{2} + 2 \right) v^2 + \left(\frac{\beta_{17}}{3} + \frac{\beta_{18}}{6} - \frac{\beta_{19}}{2} + 2 \right) w^2 \right] \\ + (3 + \gamma_{20})\partial_x(uv) + (3 + \gamma_{21})\partial_z(vw) = -\frac{s_{11}}{\rho_0\delta_t}\varepsilon m_{11}^{(1)}, \end{aligned} \quad (19\text{b})$$

$$\begin{aligned} \partial_z \left[\left(\frac{\alpha_{17}}{3} + 6c_s^2 - \frac{8}{3} \right) \delta\rho + \left(\frac{\beta_{17}}{3} - \frac{\beta_{18}}{3} + 2 \right) u^2 + \left(\frac{\beta_{17}}{3} + \frac{\beta_{18}}{6} - \frac{\beta_{19}}{2} + 2 \right) v^2 + \left(\frac{\beta_{17}}{3} + \frac{\beta_{18}}{6} + \frac{\beta_{19}}{2} + 2 \right) w^2 \right] \\ + (3 + \gamma_{22})\partial_x(uw) + (3 + \gamma_{21})\partial_y(vw) = -\frac{s_{12}}{\rho_0\delta_t}\varepsilon m_{12}^{(1)}, \end{aligned} \quad (19\text{c})$$

velocity gradients and pressure gradients. In this section, we will explore those 23 moment equations in terms of increasing order in moments to determine if the mesoscopic vorticity calculation can be made possible.

First, the six equations governing the second-order moments m_4 to m_9 can be expanded from Eq. (7b) as

$$\left(\frac{5 - 9c_s^2}{3} \right) (\partial_x u + \partial_y v + \partial_z w) = -\frac{s_4}{\rho_0\delta_t}\varepsilon m_4^{(1)}, \quad (18\text{a})$$

$$\frac{2}{3} (2\partial_x u - \partial_y v - \partial_z w) = -\frac{s_5}{\rho_0\delta_t}\varepsilon m_5^{(1)}, \quad (18\text{b})$$

$$\frac{2}{3} (\partial_y v - \partial_z w) = -\frac{s_6}{\rho_0\delta_t}\varepsilon m_6^{(1)}, \quad (18\text{c})$$

$$\frac{1}{3} (\partial_x v + \partial_y u) = -\frac{s_7}{\rho_0\delta_t}\varepsilon m_7^{(1)}, \quad (18\text{d})$$

$$\frac{1}{3} (\partial_y w + \partial_z v) = -\frac{s_8}{\rho_0\delta_t}\varepsilon m_8^{(1)}, \quad (18\text{e})$$

$$\frac{1}{3} (\partial_x w + \partial_z u) = -\frac{s_9}{\rho_0\delta_t}\varepsilon m_9^{(1)}. \quad (18\text{f})$$

The right-hand side of each of the above equations contains the leading order part of a second-order nonequilibrium moment, while the left-hand side is the spatial derivatives of the first- and third-order equilibrium moments. The time derivative in each equation has been absorbed into the spatial derivatives by using the Euler equations. Also note that terms on the order of $O(\text{Ma}^3)$ have been eliminated from the equations. Clearly, the six strain-rate components can be explicitly solved from the above six equations. Because both first- and third-order equilibrium moments on the left-hand side are defined isotropically with respect to x , y , and z , as required by the N-S equations, the nonequilibrium parts of the six second-order moments on the right-hand side involve no vorticity components. To realize explicitly the local vorticity calculation, we need to find another three independent equations involving the six cross velocity gradients $\partial_x v$, $\partial_x w$, $\partial_y u$, $\partial_y w$, $\partial_z u$, and $\partial_z v$.

Next, we exploit the moment equations for the seven third-order moments. Those equations do not appear in the inverse design process as the nonequilibrium parts of third-order moments are irrelevant to the derivation of the N-S equations, and they are

$$\left(\frac{2}{3} + \frac{\beta_{19}}{3}\right)\partial_x(v^2 - w^2) + \left(\frac{1}{3} - \frac{\gamma_{20}}{3}\right)\partial_y(uv) + \left(\frac{\gamma_{22}}{3} - \frac{1}{3}\right)\partial_z(uw) = -\frac{s_{13}}{\rho_0\delta_t}\varepsilon m_{13}^{(1)}, \quad (19d)$$

$$\left(\frac{\gamma_{20}}{3} - \frac{1}{3}\right)\partial_x(uv) - \left(\frac{\beta_{18}}{6} + \frac{1}{3}\right)\partial_y(2u^2 - v^2 - w^2) - \left(\frac{\beta_{19}}{6} + \frac{1}{3}\right)\partial_y(v^2 - w^2) + \left(\frac{1}{3} - \frac{\gamma_{21}}{3}\right)\partial_z(vw) = -\frac{s_{14}}{\rho_0\delta_t}\varepsilon m_{14}^{(1)}, \quad (19e)$$

$$\left(\frac{1}{3} - \frac{\gamma_{22}}{3}\right)\partial_x(uw) + \left(\frac{\gamma_{21}}{3} - \frac{1}{3}\right)\partial_y(vw) + \left(\frac{\beta_{18}}{6} + \frac{1}{3}\right)\partial_z(2u^2 - v^2 - w^2) - \left(\frac{\beta_{19}}{6} + \frac{1}{3}\right)\partial_z(v^2 - w^2) = -\frac{s_{15}}{\rho_0\delta_t}\varepsilon m_{15}^{(1)}, \quad (19f)$$

$$\left(\frac{2}{3} + \frac{\gamma_{21}}{3}\right)\partial_x(vw) + \left(\frac{2}{3} + \frac{\gamma_{22}}{3}\right)\partial_y(uw) + \left(\frac{2}{3} + \frac{\gamma_{20}}{3}\right)\partial_z(uv) = -\frac{s_{16}}{\rho_0\delta_t}\varepsilon m_{16}^{(1)}. \quad (19g)$$

The left-hand side of these seven equations are spatial derivatives of second- and fourth-order equilibrium moments. Again, the time derivatives are replaced by the spatial derivatives using the Euler equations. Compared to that of Eq. (18), the left-hand side of above seven equations are on higher order in Ma, i.e., the spatial derivatives in Eq. (19) scale as $O(\text{Ma}^2)$, whereas those in Eq. (18) are of $O(\text{Ma})$. For this reason, Eq. (19) is evidently not suitable to serve as desired supplementary equations for the local vorticity calculation. However, Eqs. (19a) to (19c) contain pressure gradients $\partial_x\delta\rho$, $\partial_y\delta\rho$, and $\partial_z\delta\rho$, they can be utilized to calculate pressure gradients mesoscopically if the coefficient $\alpha_{17}/3 + 6c_s^2 - 8/3$ is nonzero. In our model, α_{17} is tunable, so this direct computation of pressure gradient is achievable, in contrast with the standard LBGK model, where α_{17} must be set to 2 in order to reproduce the N-S equations. In this work, since we focus on exploring the mesoscopic vorticity calculation, the above point will not be examined further.

Now we move to the six equations of fourth-order moments, which read explicitly as

$$\left(\frac{2\xi_{23}}{3} - \frac{4}{3} - \alpha_{17}\right)\partial_x u + \left(\frac{2\xi_{24}}{3} - \frac{4}{3} - \alpha_{17}\right)\partial_y v + \left(\frac{2\xi_{25}}{3} - \frac{4}{3} - \alpha_{17}\right)\partial_z w = -\frac{s_{17}}{\rho_0\delta_t}\varepsilon m_{17}^{(1)}, \quad (20a)$$

$$-\left(\frac{2}{3} + \frac{2\xi_{23}}{3}\right)\partial_x u + \left(\frac{1}{3} + \frac{\xi_{24}}{3}\right)\partial_y v + \left(\frac{1}{3} + \frac{\xi_{25}}{3}\right)\partial_z w = -\frac{s_{18}}{\rho_0\delta_t}\varepsilon m_{18}^{(1)}, \quad (20b)$$

$$-\left(\frac{1}{3} + \frac{\xi_{24}}{3}\right)\partial_y v + \left(\frac{1}{3} + \frac{\xi_{25}}{3}\right)\partial_z w = -\frac{s_{19}}{\rho_0\delta_t}\varepsilon m_{19}^{(1)}, \quad (20c)$$

$$\left(\frac{\xi_{24}}{3} - \frac{2}{3}\right)\partial_x v + \left(\frac{\xi_{23}}{3} - \frac{2}{3}\right)\partial_y u = -\frac{s_{20}}{\rho_0\delta_t}\varepsilon m_{20}^{(1)}, \quad (20d)$$

$$\left(\frac{\xi_{25}}{3} - \frac{2}{3}\right)\partial_y w + \left(\frac{\xi_{24}}{3} - \frac{2}{3}\right)\partial_z v = -\frac{s_{21}}{\rho_0\delta_t}\varepsilon m_{21}^{(1)}, \quad (20e)$$

$$\left(\frac{\xi_{23}}{3} - \frac{2}{3}\right)\partial_z u + \left(\frac{\xi_{25}}{3} - \frac{2}{3}\right)\partial_x w = -\frac{s_{22}}{\rho_0\delta_t}\varepsilon m_{22}^{(1)}, \quad (20f)$$

where the nonequilibrium parts of fourth-order moments on the right-hand side are related to the spatial derivatives of third- and fifth-order equilibrium moments on the left-hand side. In particular, Eqs. (20d) to (20f) not only involve the cross-velocity gradients but also are on the order of $O(\text{Ma})$, the same as in Eqs. (18d) to (18f). Unlike the third-order equilibrium moments that must have full isotropy to reproduce the N-S equations, the fifth-order equilibrium moments are not constrained so they can be purposely designed to be anisotropic with $\xi_{23} \neq \xi_{24} \neq \xi_{25}$. By having anisotropic fifth-order equilibrium moments, we embed the three local vorticity components into the fourth-order nonequilibrium moments. Mathematically, when $\xi_{23} \neq \xi_{24} \neq \xi_{25}$, Eqs. (20d) to (20f) become linearly independent of Eqs. (18d) to (18f), and thus all three vorticity components can be explicitly calculated as

$$\omega_x \equiv \partial_y w - \partial_z v = \frac{1}{(\xi_{24} - \xi_{25})} \left[-\frac{3(\xi_{24} + \xi_{25} - 4)s_8}{\rho_0\delta_t}\varepsilon m_8^{(1)} + \frac{6s_{21}}{\rho_0\delta_t}\varepsilon m_{21}^{(1)} \right], \quad (21a)$$

$$\omega_y \equiv \partial_z u - \partial_x w = \frac{1}{(\xi_{25} - \xi_{23})} \left[-\frac{3(\xi_{25} + \xi_{23} - 4)s_9}{\rho_0\delta_t}\varepsilon m_9^{(1)} + \frac{6s_{22}}{\rho_0\delta_t}\varepsilon m_{22}^{(1)} \right], \quad (21b)$$

$$\omega_z \equiv \partial_x v - \partial_y u = \frac{1}{(\xi_{23} - \xi_{24})} \left[-\frac{3(\xi_{23} + \xi_{24} - 4)s_7}{\rho_0\delta_t}\varepsilon m_7^{(1)} + \frac{6s_{20}}{\rho_0\delta_t}\varepsilon m_{20}^{(1)} \right]. \quad (21c)$$

Together with Eqs. (18a) to (18f), all the velocity gradients can be explicitly determined from the nonequilibrium moments. In fact, when the number of lattice particle velocities is sufficient, the LB model can be designed to entail all the hydrodynamic quantities we are concerned with in the

CFD (i.e., velocity, pressure, velocity gradients, pressure gradients) into their mesoscopic distribution functions. The reason that such properties were never fully explored might be due to the fact that, when the LBM was first established, its equilibrium was obtained via the Taylor expansion of the

Maxwell-Boltzmann distribution at small Ma. Such design, while having the most solid physical background from the kinetic theory viewpoint, is only a sufficient but not necessary condition for the isothermal N-S equations.

In the standard LBGK model, Eq. (21) is unachievable since the isotropic equilibrium distribution function will always yield $\zeta_{23} = \zeta_{24} = \zeta_{25} = 1$. However, these values from the standard LBGK model set up a baseline to determine $\zeta_{23,24,25}$ in our model in order to ensure sufficient numerical stability. We suggest $\zeta_{23} \approx \zeta_{24} \approx \zeta_{25} \approx 1$ so we can maintain the nonequilibrium parts of second- and fourth-order moments small in terms of the same physical velocity gradients, as indicated in Eq. (21). The three numerical benchmark cases shown in Sec. IV show that the range of $0.5 \leq \zeta_{23-25} \leq 2.0$ is numerically stable, which is quite acceptable.

C. Accuracy of the mesoscopic vorticity calculation

In this section, we provide an asymptotic analysis, in terms of incompressible N-S equations, concerning the accuracy

$$f_\alpha^{(\text{eq})} = w_\alpha \delta\rho + w_\alpha \rho_0 \left\{ \frac{3[b(\alpha,1)e_{\alpha 1}u_1 + b(\alpha,2)e_{\alpha 2}u_2 + b(\alpha,3)e_{\alpha 3}u_3]}{c^2} + \frac{9(e_{\alpha i}u_i)^2}{2c^4} + \frac{3u_iu_i}{2c^2} \right\}, \quad (23)$$

which is identical to Eq. (16) except that the first term in the square brackets is designed to be anisotropic with respect to the spatial direction i . The detailed form of $b(\alpha,i)$ is provided in the Appendix in terms of three coefficients only, namely ζ'_1 , ζ'_2 and ζ'_3 [see Eqs. (A2) to (A4)]. Note that here $\zeta'_1 = \zeta_{23}$, $\zeta'_2 = \zeta_{24}$, and $\zeta'_3 = \zeta_{25}$, respectively. When $b(\alpha,1) \neq b(\alpha,2) \neq b(\alpha,3)$, the usual isotropy in the standard LBGK equilibrium is no longer assumed. However, the symmetry is still rigorously preserved, i.e., $b(\bar{\alpha},i) = b(\alpha,i)$, where $\mathbf{e}_{\bar{\alpha}} = -\mathbf{e}_\alpha$.

While the previous design is based on the C-E analysis (acoustic scaling), in the limit of incompressible flow the alternative diffusive scaling can be applied [9,31]. Under the diffusive scaling, i.e., $\delta_x = h$, $\delta_t = h^2$, $c = \delta_x/\delta_t = 1/h$, Eq. (23) can be rewritten as

$$f_\alpha^{(\text{eq})} = h^2 w_\alpha \tilde{\rho} + 3h w_\alpha \rho_0 [b(\alpha,1)e_{\alpha 1}u_1 + b(\alpha,2)e_{\alpha 2}u_2 + b(\alpha,3)e_{\alpha 3}u_3] + \frac{9}{2}h^2 w_\alpha \rho_0 (e_{\alpha i}u_i)^2 + \frac{3}{2}h^2 w_\alpha \rho_0 u_i u_i. \quad (24)$$

where the density fluctuation $\delta\rho = h^2 \tilde{\rho}$ is on the order of $O(h^2)$ in the incompressible limit.

Applying Taylor expansion to the left-hand side of Eq. (22), we obtain

$$\sum_{s=1}^{\infty} h^s D_{\alpha,s} f_\alpha(\mathbf{x},t) = -\frac{1}{\tau} [f_\alpha(\mathbf{x},t) - f_\alpha^{(\text{eq})}(\mathbf{x},t)], \quad D_{\alpha,s} = \sum_{m+2n=s} \frac{\partial_t^n (\mathbf{e}_\alpha \cdot \nabla)^m}{m! n!}. \quad (25)$$

Expanding the left-hand side of Eq. (25) to $O(h^4)$, the following relation between f_α and $f_\alpha^{(\text{eq})}$ is obtained:

$$f_\alpha - f_\alpha^{(\text{eq})} = -\tau [h(\mathbf{e}_\alpha \cdot \nabla) f_\alpha + \frac{1}{2}h^2(\mathbf{e}_\alpha \cdot \nabla)^2 f_\alpha + \frac{1}{6}h^3(\mathbf{e}_\alpha \cdot \nabla)^3 f_\alpha + h^2 \partial_t f_\alpha + h^3(\mathbf{e}_\alpha \cdot \nabla) \partial_t f_\alpha] + O(h^4). \quad (26)$$

Note that we have simplified the notations since all terms in the above equation is at (\mathbf{x},t) . Now we process the Maxwell iteration, i.e., substitute Eq. (26) into itself and again keep all the terms to $O(h^4)$, and we can express f_α in terms of $f_\alpha^{(\text{eq})}$ as

$$\begin{aligned} f_\alpha - f_\alpha^{(\text{eq})} &= -\tau h(\mathbf{e}_\alpha \cdot \nabla) f_\alpha^{(\text{eq})} + \tau^2 h^2(\mathbf{e}_\alpha \cdot \nabla)^2 f_\alpha^{(\text{eq})} - \tau \frac{1}{2}h^2(\mathbf{e}_\alpha \cdot \nabla)^2 f_\alpha^{(\text{eq})} - \tau^3 h^3(\mathbf{e}_\alpha \cdot \nabla)^3 f_\alpha^{(\text{eq})} \\ &\quad + \tau^2 h^3(\mathbf{e}_\alpha \cdot \nabla)^3 f_\alpha^{(\text{eq})} + 2\tau^2 h^3(\mathbf{e}_\alpha \cdot \nabla) \partial_t f_\alpha^{(\text{eq})} - \tau h^3(\mathbf{e}_\alpha \cdot \nabla) \partial_t f_\alpha^{(\text{eq})} - \tau \frac{1}{6}h^3(\mathbf{e}_\alpha \cdot \nabla)^3 f_\alpha^{(\text{eq})} + O(h^4). \end{aligned} \quad (27)$$

Finally, substituting Eq. (24) into Eq. (27), we have

$$\begin{aligned} f_\alpha - f_\alpha^{(\text{eq})} &= -3w_\alpha \rho_0 \tau h^2(\mathbf{e}_\alpha \cdot \nabla) [b(\alpha,1)e_{\alpha 1}u_1 + b(\alpha,2)e_{\alpha 2}u_2 + b(\alpha,3)e_{\alpha 3}u_3] - w_\alpha \tau h^3(\mathbf{e}_\alpha \cdot \nabla) [\tilde{\rho} + \frac{9}{2}\rho_0 (e_{\alpha i}u_i)^2 + \frac{3}{2}\rho_0 u_i u_i] \\ &\quad + 3w_\alpha \rho_0 (\tau - \frac{1}{2})h^3(\mathbf{e}_\alpha \cdot \nabla)^2 [b(\alpha,1)e_{\alpha 1}u_1 + b(\alpha,2)e_{\alpha 2}u_2 + b(\alpha,3)e_{\alpha 3}u_3] + O(h^4). \end{aligned} \quad (28)$$

Clearly, the right-hand side of Eq. (28) contains an even part in terms of \mathbf{e}_α , which is the first term, and an odd part that consist of all the remaining terms. When multiplied by

of our proposed mesoscopic vorticity calculation following the idea of the Maxwell iteration [29,30]. To simplify the analysis, all the relaxation times in our model are chosen identical to be $1/\tau$ since their values are not essential in the vorticity calculation. Furthermore, since only three coefficients of fifth-order equilibrium moments are relevant to the vorticity calculation, other undefined coefficients of fourth-order and sixth-order equilibrium moments are chosen corresponding to the standard LBGK equilibrium, namely $\alpha_{17} = 2$, $\beta_{17} = -4$, $\beta_{18} = \beta_{19} = -1$, $\gamma_{20} = \gamma_{21} = \gamma_{22} = -1$, $\alpha_{26} = -1$, $\beta_{26} = 3$. The evolution equation, Eq. (4), can then be simplified as

$$f_\alpha(\mathbf{x} + \mathbf{e}_\alpha \delta_t, t + \delta_t) - f_\alpha(\mathbf{x}, t) = -\frac{1}{\tau} [f_\alpha(\mathbf{x}, t) - f_\alpha^{(\text{eq})}(\mathbf{x}, t)], \quad (22)$$

where the equilibrium distribution $\mathbf{f}^{(\text{eq})} = \mathbf{M}^{-1} \mathbf{m}^{(\text{eq})}$. Based on the design in Eqs. (10), (15), and (17), it can be shown that the equilibrium distribution can be written as

$$f_\alpha^{(\text{eq})} = w_\alpha \delta\rho + w_\alpha \rho_0 \left\{ \frac{3[b(\alpha,1)e_{\alpha 1}u_1 + b(\alpha,2)e_{\alpha 2}u_2 + b(\alpha,3)e_{\alpha 3}u_3]}{c^2} + \frac{9(e_{\alpha i}u_i)^2}{2c^4} + \frac{3u_iu_i}{2c^2} \right\}, \quad (23)$$

which is identical to Eq. (16) except that the first term in the square brackets is designed to be anisotropic with respect to the spatial direction i . The detailed form of $b(\alpha,i)$ is provided in the Appendix in terms of three coefficients only, namely ζ'_1 , ζ'_2 and ζ'_3 [see Eqs. (A2) to (A4)]. Note that here $\zeta'_1 = \zeta_{23}$, $\zeta'_2 = \zeta_{24}$, and $\zeta'_3 = \zeta_{25}$, respectively. When $b(\alpha,1) \neq b(\alpha,2) \neq b(\alpha,3)$, the usual isotropy in the standard LBGK equilibrium is no longer assumed. However, the symmetry is still rigorously preserved, i.e., $b(\bar{\alpha},i) = b(\alpha,i)$, where $\mathbf{e}_{\bar{\alpha}} = -\mathbf{e}_\alpha$.

While the previous design is based on the C-E analysis (acoustic scaling), in the limit of incompressible flow the alternative diffusive scaling can be applied [9,31]. Under the diffusive scaling, i.e., $\delta_x = h$, $\delta_t = h^2$, $c = \delta_x/\delta_t = 1/h$, Eq. (23) can be rewritten as

$$f_\alpha^{(\text{eq})} = h^2 w_\alpha \tilde{\rho} + 3h w_\alpha \rho_0 [b(\alpha,1)e_{\alpha 1}u_1 + b(\alpha,2)e_{\alpha 2}u_2 + b(\alpha,3)e_{\alpha 3}u_3] + \frac{9}{2}h^2 w_\alpha \rho_0 (e_{\alpha i}u_i)^2 + \frac{3}{2}h^2 w_\alpha \rho_0 u_i u_i. \quad (24)$$

where the density fluctuation $\delta\rho = h^2 \tilde{\rho}$ is on the order of $O(h^2)$ in the incompressible limit.

Applying Taylor expansion to the left-hand side of Eq. (22), we obtain

$$\sum_{s=1}^{\infty} h^s D_{\alpha,s} f_\alpha(\mathbf{x},t) = -\frac{1}{\tau} [f_\alpha(\mathbf{x},t) - f_\alpha^{(\text{eq})}(\mathbf{x},t)], \quad D_{\alpha,s} = \sum_{m+2n=s} \frac{\partial_t^n (\mathbf{e}_\alpha \cdot \nabla)^m}{m! n!}. \quad (25)$$

Expanding the left-hand side of Eq. (25) to $O(h^4)$, the following relation between f_α and $f_\alpha^{(\text{eq})}$ is obtained:

$$f_\alpha - f_\alpha^{(\text{eq})} = -\tau [h(\mathbf{e}_\alpha \cdot \nabla) f_\alpha + \frac{1}{2}h^2(\mathbf{e}_\alpha \cdot \nabla)^2 f_\alpha + \frac{1}{6}h^3(\mathbf{e}_\alpha \cdot \nabla)^3 f_\alpha + h^2 \partial_t f_\alpha + h^3(\mathbf{e}_\alpha \cdot \nabla) \partial_t f_\alpha] + O(h^4). \quad (26)$$

Note that we have simplified the notations since all terms in the above equation is at (\mathbf{x},t) . Now we process the Maxwell iteration, i.e., substitute Eq. (26) into itself and again keep all the terms to $O(h^4)$, and we can express f_α in terms of $f_\alpha^{(\text{eq})}$ as

$$\begin{aligned} f_\alpha - f_\alpha^{(\text{eq})} &= -\tau h(\mathbf{e}_\alpha \cdot \nabla) f_\alpha^{(\text{eq})} + \tau^2 h^2(\mathbf{e}_\alpha \cdot \nabla)^2 f_\alpha^{(\text{eq})} - \tau \frac{1}{2}h^2(\mathbf{e}_\alpha \cdot \nabla)^2 f_\alpha^{(\text{eq})} - \tau^3 h^3(\mathbf{e}_\alpha \cdot \nabla)^3 f_\alpha^{(\text{eq})} \\ &\quad + \tau^2 h^3(\mathbf{e}_\alpha \cdot \nabla)^3 f_\alpha^{(\text{eq})} + 2\tau^2 h^3(\mathbf{e}_\alpha \cdot \nabla) \partial_t f_\alpha^{(\text{eq})} - \tau h^3(\mathbf{e}_\alpha \cdot \nabla) \partial_t f_\alpha^{(\text{eq})} - \tau \frac{1}{6}h^3(\mathbf{e}_\alpha \cdot \nabla)^3 f_\alpha^{(\text{eq})} + O(h^4). \end{aligned} \quad (27)$$

Finally, substituting Eq. (24) into Eq. (27), we have

$$\begin{aligned} f_\alpha - f_\alpha^{(\text{eq})} &= -3w_\alpha \rho_0 \tau h^2(\mathbf{e}_\alpha \cdot \nabla) [b(\alpha,1)e_{\alpha 1}u_1 + b(\alpha,2)e_{\alpha 2}u_2 + b(\alpha,3)e_{\alpha 3}u_3] - w_\alpha \tau h^3(\mathbf{e}_\alpha \cdot \nabla) [\tilde{\rho} + \frac{9}{2}\rho_0 (e_{\alpha i}u_i)^2 + \frac{3}{2}\rho_0 u_i u_i] \\ &\quad + 3w_\alpha \rho_0 (\tau - \frac{1}{2})h^3(\mathbf{e}_\alpha \cdot \nabla)^2 [b(\alpha,1)e_{\alpha 1}u_1 + b(\alpha,2)e_{\alpha 2}u_2 + b(\alpha,3)e_{\alpha 3}u_3] + O(h^4). \end{aligned} \quad (28)$$

Clearly, the right-hand side of Eq. (28) contains an even part in terms of \mathbf{e}_α , which is the first term, and an odd part that consist of all the remaining terms. When multiplied by

for any second- and fourth-order moment, the leading-order truncation error in its nonequilibrium part is on the order of $O(h^4)$ since all $O(h^3)$ terms in Eq. (28) disappear due to the symmetry in terms of the lattice velocities. As shown in Eqs. (18) and (21), the computation of all velocity gradients in the present model only involves even order nonequilibrium moments. Thus, the mesoscopic velocity gradient calculation indeed has the second-order accuracy.

An interesting question to ask is whether the same design can be achieved with D3Q15 or D3Q19 lattice grids. In our D3Q27 lattice model, the mesoscopic vorticity calculation is made possible by introducing anisotropy into the three fifth-order equilibrium moments. However, as shown in Ref. [20], in D3Q15 there are only one zeroth-order moment, three first-order moments, six second-order moments, four third-order moments, and one fourth-order moment; while in D3Q19 there are only one zeroth-order moment, three first-order moments, six second-order moments, sixth third-order moments, and three fourth-order moments. The fifth-order moments available to D3Q27 simply do not exist in D3Q15 and D3Q19. Therefore, we conclude that both D3Q15 and D3Q19 MRT models are not flexible enough to allow mesoscopic vorticity calculation.

IV. NUMERICAL VALIDATION AND RESULTS

In this section, the mesoscopic vorticity calculation in our model is numerically investigated in three 3D flows, i.e., a 3D Taylor-Green vortex flow, a 3D lid-driven cavity flow, and a uniform flow passing a fixed sphere. The main purposes of those examinations are (1) to numerically prove the modification on the fifth-order equilibrium moments brings only marginal effect to the numerical accuracy and stability of LBM as a N-S equation solver and (2) to validate the accuracy of mesoscopic vorticity calculation.

A. The 3D Taylor-Green vortex flow

The 3D Taylor-Green vortex flow is one of the very few analytical solutions of three-dimensional time-dependent N-S equations. In 1936, Taylor and Green [32] established the short-time solution based on a perturbation expansion of the velocity field. Given the initial velocity field $\mathbf{u}_0 = (u_0, v_0, w_0)$,

$$u_0(x, y, z, t=0) = U_0 \cos(2\pi x/L) \sin(2\pi y/L) \sin(2\pi z/L), \quad (29a)$$

$$v_0(x, y, z, t=0) = -U_0 \sin(2\pi x/L) \cos(2\pi y/L) \times \sin(2\pi z/L), \quad (29b)$$

$$w_0(x, y, z, t=0) = 0, \quad (29c)$$

where $0 \leq x \leq L$, $0 \leq y \leq L$, $0 \leq z \leq L$ are the spatial coordinates, L is the domain size, t is time, and U_0 is the initial characteristic velocity magnitude. Periodic boundary conditions are assumed in all three directions. The initial velocity gradients are known analytically and the initial pressure field can also be obtained by solving the Poisson equation. The time derivative of velocities in the N-S equations can be expressed in terms of the initial velocity and pressure fields, which can be integrated to give a short-time

TABLE I. The physical and simulation parameters in the 3D Taylor-Green flow

| Case # | Re_0 | $N_x \times N_y \times N_z$ | U_0 | ν | ν^V |
|--------|----------|-----------------------------|--------|---------|---------|
| 1 | 600π | $64 \times 64 \times 64$ | 0.1019 | 0.00346 | 0.0370 |
| 2 | 600π | $128 \times 128 \times 128$ | 0.0509 | 0.00346 | 0.0370 |
| 3 | 600π | $256 \times 256 \times 256$ | 0.0255 | 0.00346 | 0.0370 |

solution. Repeat the above iteration process of velocity field \rightarrow pressure field \rightarrow velocity time derivatives \rightarrow updated velocity field, Taylor and Green obtained a three-dimensional, time-dependent theoretical solution that is valid for short times [32]. Based on this solution, analytical expressions of kinetic energy and dissipation rate at short times were also obtained in Ref. [32].

In this section, we focus on benchmarking the vorticity field obtained from the moment equations presented in Sec. III B. However, the theoretical solution derived by Taylor and Green will not be used as the benchmark due to the reason that it is only valid for short times. It is difficult to determine precisely how long the theoretical solution is accurate enough to be used as benchmark, which depends on which physical quantity is of concern. Instead, the solution from a pseudospectral method (PSM) is used as benchmark for its high-accuracy with an exponential convergence rate. In the past, the PSM results have often been used to benchmark results from LBM [5,7,21].

Some of the key parameters adopted in the present MRT LBM are listed in Tables I and II. For all three cases, the initial Reynolds number $Re_0 = U_0 L / \nu$ is set to 600π so the small scales can develop relatively quickly by nonlinear interactions. Also, since we are mainly interested in the mesoscopic vorticity calculation, which only involves three coefficients, $\zeta_{23,24,25}$, we set all the other coefficients of high-order equilibrium moments to the ones that recovers LBGK equilibrium. In particular, the potential capability of mesoscopic pressure gradient calculation will not be exposed in the present study as α_{17} is still set to 2 in all cases. On the other hand, the values of $\zeta_{23,24,25}$ as well as the relaxation parameters of third- and higher-order moments are chosen rather casually (we avoid extreme values though) for demonstrative purpose. Optimization of those parameters could lead to better accuracy and stability the model, but it is beyond the scope of the present study.

To properly specify all the initial particle distributions, we need to iterate the distribution functions [33]. The detailed procedure is as follows [33].

TABLE II. The coefficients of high-order equilibrium moments and relaxation parameters in the Taylor-Green flow simulations (identical in all three cases).

| α_{17} | β_{17} | $\beta_{18,19}$ | $\gamma_{20,21,22}$ | ζ_{23} | ζ_{24} | ζ_{25} | α_{26} | β_{26} |
|---------------|------------------|-----------------|---------------------|--------------|--------------|--------------|---------------|--------------|
| 2.0 | -4.0 | -1.0 | -1.0 | 1.0 | 1.5 | 2.0 | -1.0 | 3.0 |
| s_4 | s_{5-9} | s_{10-12} | s_{13-16} | s_{17-22} | s_{23} | s_{24} | s_{25} | s_{26} |
| 1.5 | $1/(3\nu + 0.5)$ | 1.2 | 1.2 | 1.5 | 1.2 | 1.2 | 1.2 | 1.2 |

(1) First, initialize the distributions by the equilibrium distribution functions based on the initial velocity field and uniform zero pressure field as $\mathbf{f}_0 = \mathbf{M}^{-1}\mathbf{m}^{(\text{eq})}(\delta\rho = 0, \mathbf{u}_0)$.

(2) Evolve the distribution function, for one time step, according to the standard collision and streaming substeps, i.e., $\mathbf{f}_0 \rightarrow \mathbf{f}^*$.

(3) Restore the initial velocity field by first converting the distributions to the moment space through $\mathbf{m} = \mathbf{M}\mathbf{f}^*$, then set $m_1 = \rho_0 u_0$, $m_2 = \rho_0 v_0$, $m_3 = \rho_0 w_0$, finally update the distributions by an inverse transform $\mathbf{f}_0 = \mathbf{M}^{-1}\mathbf{m}$. It is worth mentioning that in the later convergence rate calibration of strain rate and vorticity calculation, we also restore all the velocity gradient components back to their initial values in order to ensure that the initialization is fully consistent with the initial flow field. In other words, the nine moments that associated with the strain rate and vorticity calculation, i.e., $m_{4,5,6}$, $m_{7,8,9}$, and $m_{20,21,22}$, are also constrained using the initial velocity and velocity gradients. However, such treatment is not necessary in the usual initialization process.

(4) Repeat step 2 and step 3 for a sufficient number of iteration steps.

In the simulations, we specify the number of iteration steps. For three cases, the initial distribution functions are iterated for 1000, 4000, and 16 000 steps, respectively. The iteration numbers are chosen to be consistent with the amount of time steps the flow evolves under each grid resolution. Typically, at the end of the iteration, the maximum local pressure difference, namely $c_s^2[\delta\rho^{(m)} - \delta\rho^{(m-1)}]/(\rho_0 U_0^2)$, between two consecutive iterations, m and $m - 1$, is about 10^{-7} . It shall be noted that although in this case, the initial pressure field can be analytically obtained by solving the Poisson equation, such a pressure field based on incompressible assumption may not be consistent with the LB solution that corresponds to the weakly compressible N-S equations. Therefore, in the present simulations, we do not utilize the theoretical incompressible-flow pressure field. On the other hand, although the velocity divergence in LBM is not strictly zero, the three moments associated with the three normal velocity gradients, i.e., $m_{4,5,6}$ are still constrained. This is mainly to guarantee no significant initialization error is introduced in the later convergence study of strain rate and vorticity computations.

Before discussing the results for the flow vorticity, we first examine a few basic flow statistics to validate our model. The time-dependent kinetic energy k , dissipation rate D , and the longitudinal velocity-derivative skewness S and flatness F are shown in Fig. 2. These statistical quantities are defined as

$$k = 0.5(u^2 + v^2 + w^2), \quad (30\text{a})$$

$$D = 2\nu \left(s_{ij} - \frac{1}{3} \nabla \cdot \mathbf{u} \delta_{ij} \right)^2 + \nu^V (\nabla \cdot \mathbf{u}), \quad (30\text{b})$$

$$S = \frac{\langle \frac{1}{3}[(\partial_x u)^3 + (\partial_y v)^3 + (\partial_z w)^3] \rangle}{\langle \frac{1}{3}[(\partial_x u)^2 + (\partial_y v)^2 + (\partial_z w)^2] \rangle^{3/2}}, \quad (30\text{c})$$

$$F = \frac{\langle \frac{1}{3}[(\partial_x u)^4 + (\partial_y v)^4 + (\partial_z w)^4] \rangle}{\langle \frac{1}{3}[(\partial_x u)^2 + (\partial_y v)^2 + (\partial_z w)^2] \rangle^2}, \quad (30\text{d})$$

where s_{ij} is the strain rate tensor. The kinetic energy and dissipation rate are normalized by their respective initial

values. In the same plot, we compare the results obtained from (1) the short-time theory, as in Ref. [32], denoted as “Theory”; (2) the pseudospectral method at two different resolutions $n_x = 128$ and 256, denoted as “Spectral”; (3) the present LB model in terms of the moment equations at three different resolutions $nx = 64$, 128, and 256, denoted as “Present”; and, finally, (4) the regular MRT LB model that recovers LBGK equilibrium at resolutions $nx = 64$ and 256, denoted as “MRT,” in order to assess the impact of modifying equilibrium on the physical accuracy. The LBM results involved in the above comparisons are mesoscopically computed from the nonequilibrium moments.

As clearly shown in Fig. 2, the two groups of pseudospectral results are essentially identical, with very minor differences in skewness and flatness. Since the pseudospectral results are well converged, the PSM results at resolution 256 are viewed as the benchmark. As expected, the theoretical results are only valid for short times. Under the current setting of $Re_0 = 600\pi$, the short-time theory are quantitatively reliable for $t^* \leq 1$, where $t^* = 2\pi U_0 t / L$ is the nondimensional time. As more and more small scales develop at later times, the theory is no longer accurate, especially for the high-order statistics. On the other hand, the corresponding results of the present LB model and regular MRT LB model are in excellent agreement with each other: Both converge to the PSM data as grid resolution increases. This confirms our claim that the modification of high-order equilibrium moments only has a marginal impact on the hydrodynamics since those moments are irrelevant to the reproduction of the N-S equations.

Compared with its impacts on accuracy, modifying the high-order equilibrium moments might bring a more obvious effect on the numerical stability. To clarify, we compared the stability limits of both the present model and regular MRT model in the same case of decaying Taylor-Green flow at $Re_0 = 600\pi$ and a grid resolution of $n_x = 64$. For this unsteady flow case, more and more small scales develop with time and the simulation eventually leads unphysical results when the grid resolution fails to resolve those small scales. Therefore, we define the stability limit as the minimum shear viscosity used by the model to yield physically accurate kinetic energy in the time period of concern ($t^* \leq 10$). As shown in Fig. 3, the stability limits for both the present model and the regular MRT model are around 0.002 in terms of shear viscosity value. Decreasing the shear viscosity further, the present model tends to yield inaccurate kinetic energy earlier than the regular MRT model does, which indicates that the former has slightly worse numerical stability. However, it must be noted that in the present model, all the high-order equilibrium moments are tunable, which could potentially lead to better numerical stability. Combining those two aspects, we conclude that the modification of high-order equilibrium moments does not significantly affect the numerical stability of LB model.

Next, we validate the mesoscopic vorticity calculation in the present LB model. In the remaining part of this section, we shall use two different approaches to calculate the vorticity field from the LB simulations. The first approach is to use the finite-difference approximation (e.g., as in Ref. [12]), which could degrade the accuracy by one order from that for the velocity, as mentioned before. The errors in the

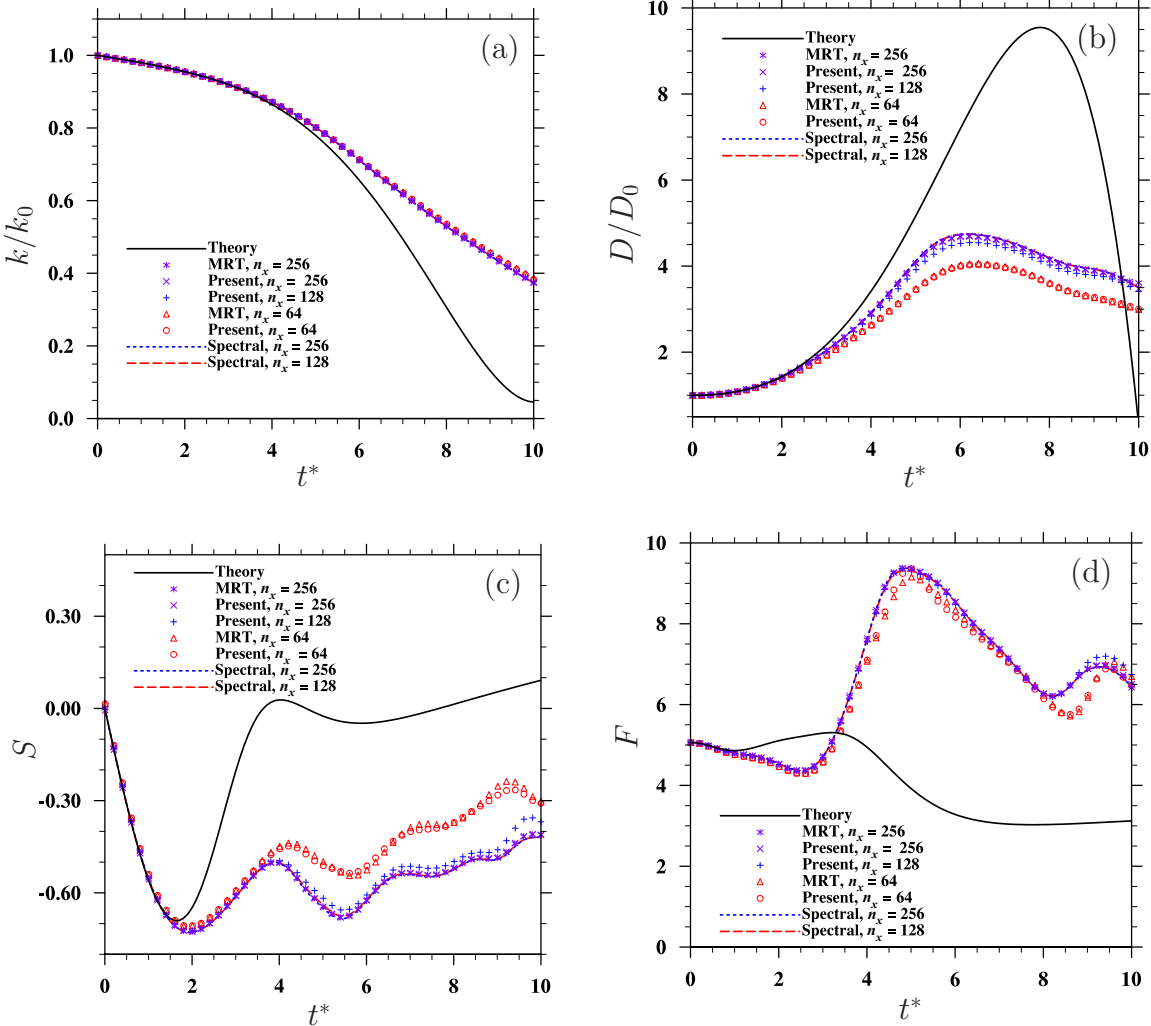


FIG. 2. The statistics in a decaying 3D Taylor-Green flow with $\text{Re}_0 = 600\pi$: (a) kinetic energy, (b) dissipation rate, (c) skewness, and (d) flatness. k_0 and D_0 are the kinetic energy and dissipation rate at the initial time, respectively.

finite-difference approximation have two origins. The first is the numerical error, which originates from the second-order

velocity error in LBM. The second is the truncation error whose order depends on the finite-difference representation we choose. It shall be clear that the latter error exists even when the velocity result is precise. In the vorticity calculation based on finite-difference approximation, we need to make sure a finite-difference scheme is at least second-order accurate. In our later calculation, a second-order central-differencing scheme using the LBM velocity field has been employed as

$$\frac{\partial u_i}{\partial x_j}(\mathbf{x}) = \frac{u_i(\mathbf{x} + \mathbf{e}_j h) - u_i(\mathbf{x} - \mathbf{e}_j h)}{2h} + O(h^2), \quad (31)$$

where h is the grid spacing and i and j are the indices of velocity direction and spatial coordination, respectively. Schemes of higher-order accuracy can be used to minimize the truncation error in the finite-difference-based vorticity calculation. Those higher-order schemes are usually based on large stencil widths that may introduce extra workload in data communication between processors in parallel computations and are hard to implement when complex boundary geometries present. There are also efforts to utilize the lattice links other than those align with the axes of a Cartesian coordinate to construct high-order discretizations of differential operators

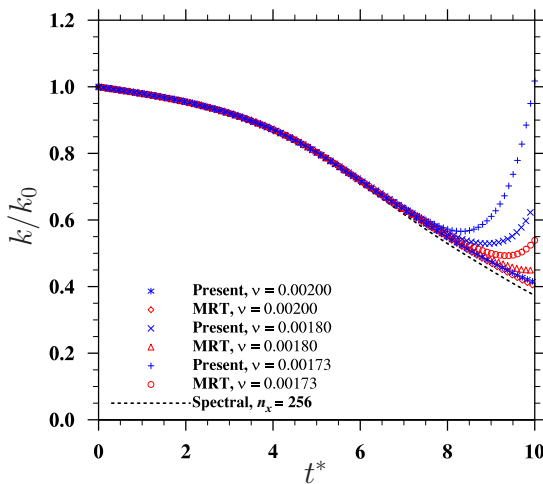


FIG. 3. The kinetic energy results of a decaying 3D Taylor-Green flow with different shear viscosities.

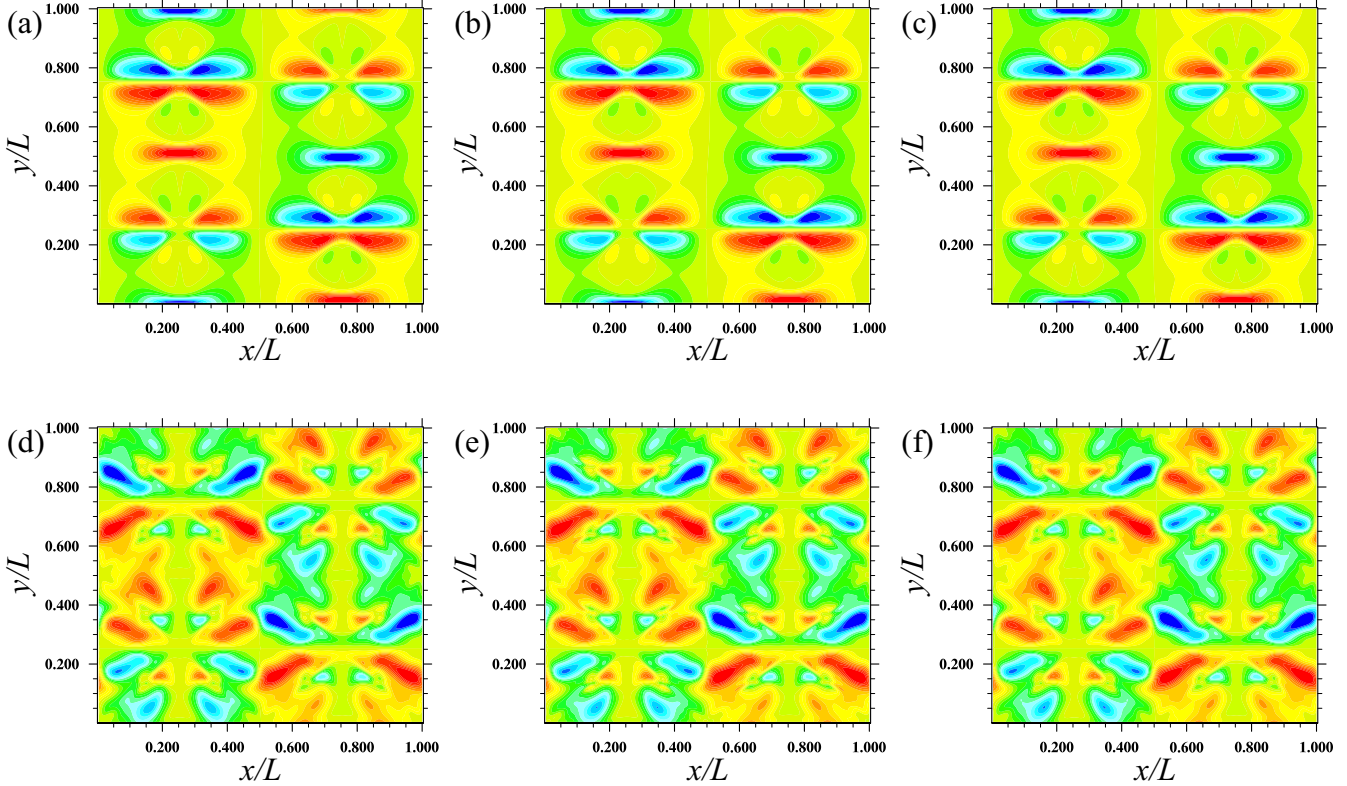


FIG. 4. Contours of vorticity in x direction at $t^* = 4$ and $t^* = 8$ with $\text{Re} = 300$ using different (a) FD, $t^* = 4$, (b) ME, $t^* = 4$, (c) PSM, $t^* = 4$, (d) FD, $t^* = 8$, (e) ME, $t^* = 8$, and (f) PSM, $t^* = 8$.

with compact stencils [34]. However, as long as the vorticity is differentiated based on the second-order-accurate velocity field, its overall order of accuracy is expected to be lower than second order. This is because the error in the velocity field is usually not distributed uniformly and does not cancel out in the differentiation scheme.

Alternatively, the vorticity can be calculated locally from the nonequilibrium moments, which is a unique capability of the present model. As a qualitative illustration, the vorticity contours of ω_x , ω_y , and ω_z on a 2D slice at $z/L = 0.5$ at $t^* = 4$ and $t^* = 8$ are presented in Figs. 4, 5, and 6, respectively. The resolution $n_x = n_y = n_z = 256$ is chosen for all results in these three figures. The vorticity results calculated from the present model with finite difference approximation and moment equations are denoted as FD and ME, respectively, while the spectral benchmarks are called PSM. As clearly shown by the three figures, the vorticity contours from the present LB model with the FD and ME approaches are almost identical, and both are in good agreement with contours from PSM. The capability of the ME approach for local vorticity calculation is thus well supported. Physically, there are more small-scale features in the vorticity field at the later times, which causes the relative magnitude of the nonequilibrium moment to increase relative to the equilibrium part in some local regions. This could lead to a better accuracy of local vorticity calculated by the mesoscopic method, provided that there are no numerical noises in these high-order nonequilibrium moments used in the mesoscopic representation of the local vorticity. This aspect needs further investigation. On the other hand, the finite-difference approximated vorticity tends

to be smoother since the velocity field in LBM is associated with the first-order equilibrium moment which does not usually contain numerical oscillations.

We shall now compute the convergence rate of both FD and ME approaches using the PSM results at highest resolution ($n_x = n_y = n_z = 256$) as the benchmark. In LBM, three resolutions $n_x = n_y = n_z = 64, 128$, and 256 are considered. For fair comparison, the LBM grids for all resolutions are aligned precisely with the PSM grid such that no interpolation is necessary. The L1 and L2 norms are computed, which are defined as

$$\varepsilon_{L1}(t) = \frac{\sum_{x,y} |q_{\text{LBM}}(x,y,t) - q_{\text{PSM}}(x,y,t)|}{\sum_{x,y} |q_{\text{PSM}}(x,y,t)|}, \quad (32a)$$

$$\varepsilon_{L2}(t) = \frac{\sqrt{\sum_{x,y} [q_{\text{LBM}}(x,y,t) - q_{\text{PSM}}(x,y,t)]^2}}{\sqrt{\sum_{x,y} [q_{\text{PSM}}(x,y,t)]^2}}, \quad (32b)$$

where q_{LBM} and q_{PSM} represent the corresponding numerical results (velocity, strain rate, vorticity, etc.) of LBM and PSM, respectively, and the summation is over the whole computational domain. At the initial stage ($t^* = 0$), the L2 error norms are shown in Table III. Here we will only show explicitly the results of L2 error norms, as the corresponding results of L1 error norms are very similar. While the L2 errors in velocity are negligibly small [$\sim O(10^{-7})$] and are almost independent of the grid resolution, implying that these errors are due to machine round-off errors. The same holds true for the errors in vorticity and strain rates computed through ME. On the other hand, the errors in vorticity and strain rates from the FD

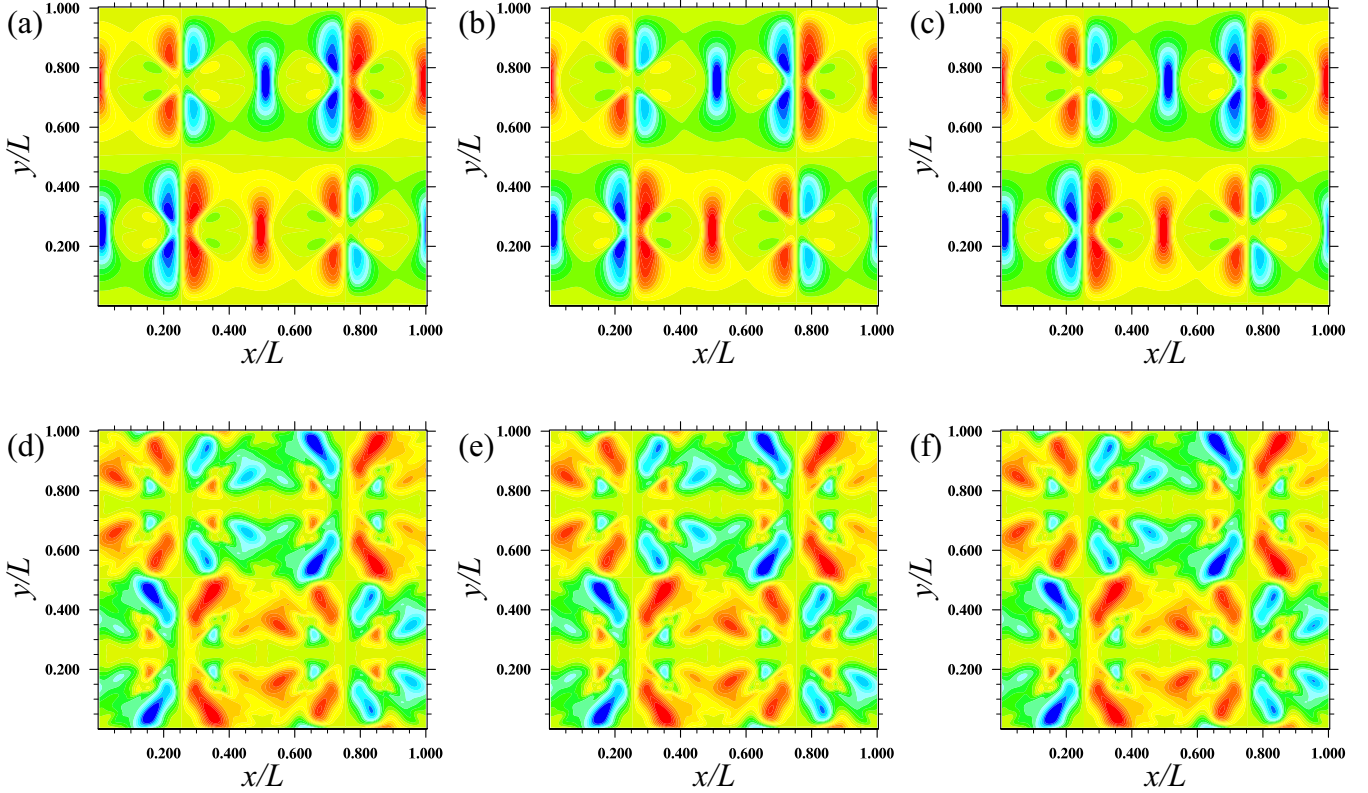


FIG. 5. Contours of vorticity in y direction at $t^* = 4$ and $t^* = 8$ with $\text{Re} = 300$ using different (a) FD, $t^* = 4$, (b) ME, $t^* = 4$, (c) PSM, $t^* = 4$, (d) FD, $t^* = 8$, (e) ME, $t^* = 8$, and (f) PSM, $t^* = 8$.

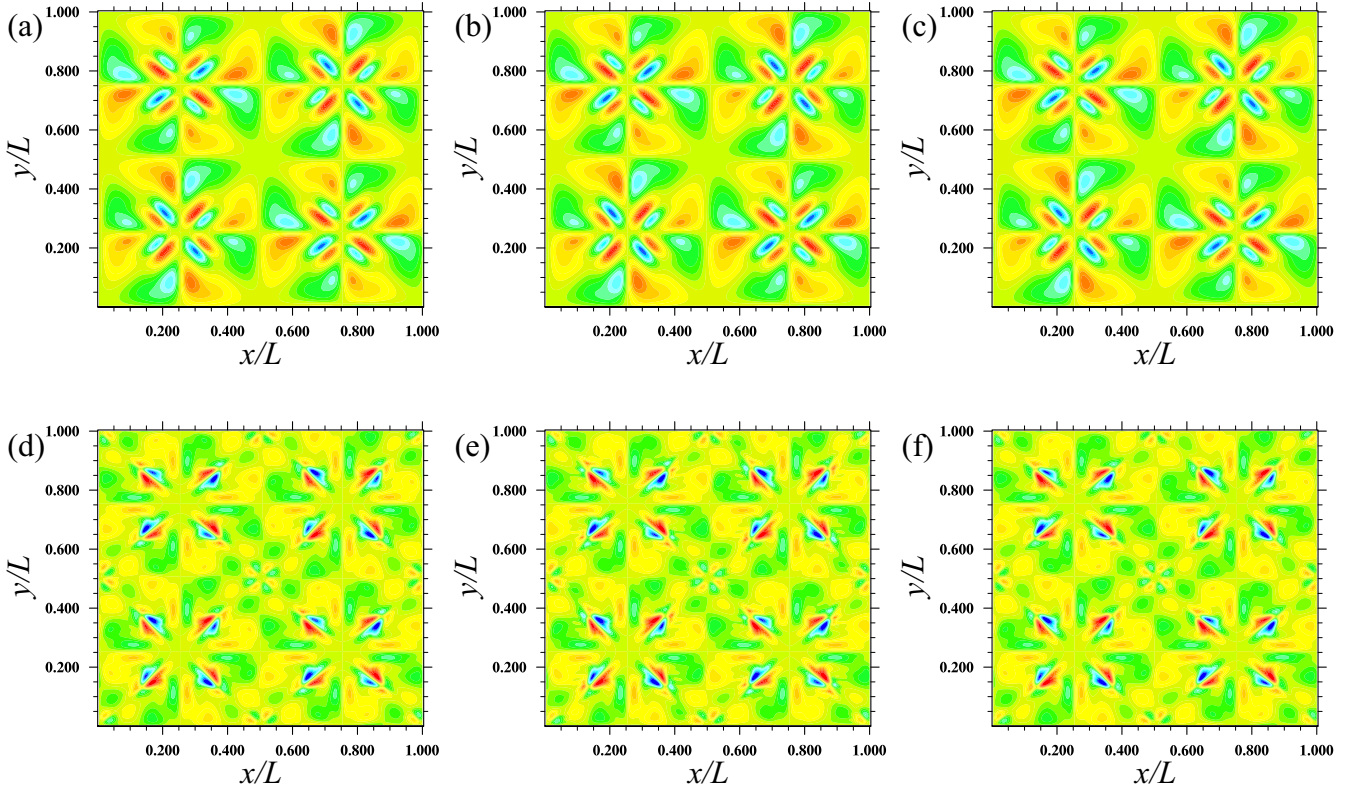


FIG. 6. Contours of vorticity in the z direction at $t^* = 4$ and $t^* = 8$ with $\text{Re} = 300$ using different (a) FD, $t^* = 4$, (b) ME, $t^* = 4$, (c) PSM, $t^* = 4$, (d) FD, $t^* = 8$, (e) ME, $t^* = 8$, and (f) PSM, $t^* = 8$.

TABLE III. The L2 norms of velocity and vorticity at the initial time ($t^* = 0$). For completeness, the L2 norms of strain rate components are also listed. The L2 norms of velocity w , strain rate $s_{zz} = \partial_z w$, and $s_{xy} = 0.5(\partial_x v + \partial_y u)$ are not given since, at the initial stage, w , s_{zz} , and s_{xy} are identically zero in the whole domain.

| n_x | u | v | w | | | | | | |
|-------|-----------------|-----------------|-----------------|-----------------|-----------------|-----------------|--|--|--|
| 64 | 6.812E-8 | 6.812E-8 | (-) | | | | | | |
| 128 | 1.120E-7 | 1.120E-7 | (-) | | | | | | |
| 256 | 1.643E-7 | 1.643E-7 | (-) | | | | | | |
| n_x | ω_x (FD) | ω_x (ME) | ω_y (FD) | ω_y (ME) | ω_z (FD) | ω_z (ME) | | | |
| 64 | 1.606E-3 | 7.266E-8 | 1.606E-3 | 7.266E-8 | 1.606E-3 | 1.731E-7 | | | |
| 128 | 4.016E-4 | 1.708E-7 | 4.016E-4 | 1.708E-7 | 4.016E-4 | 1.153E-7 | | | |
| 256 | 1.004E-4 | 1.000E-7 | 1.004E-4 | 1.000E-7 | 1.004E-4 | 1.403E-7 | | | |
| n_x | s_{xx} (FD) | s_{xx} (ME) | s_{yy} (FD) | s_{yy} (ME) | s_{zz} (FD) | s_{zz} (ME) | | | |
| 64 | 1.606E-3 | 7.266E-8 | 1.606E-3 | 7.266E-8 | (-) | (-) | | | |
| 128 | 4.016E-4 | 1.708E-7 | 4.016E-4 | 1.708E-7 | (-) | (-) | | | |
| 256 | 1.004E-4 | 1.003E-7 | 1.004E-4 | 1.003E-7 | (-) | (-) | | | |
| n_x | s_{xy} (FD) | s_{xy} (ME) | s_{yz} (FD) | s_{yz} (ME) | s_{xz} (FD) | s_{xz} (ME) | | | |
| 64 | (-) | (-) | 1.606E-3 | 1.138E-7 | 1.606E-3 | 1.138E-7 | | | |
| 128 | (-) | (-) | 4.016E-4 | 1.343E-7 | 4.016E-4 | 1.343E-7 | | | |
| 256 | (-) | (-) | 1.004E-4 | 1.533E-7 | 1.004E-4 | 1.533E-7 | | | |

approximation are on the respective order of 10^{-3} to 10^{-4} and decrease with increasing grid resolution. Since we initialize the flow with the exact initial velocity field, these errors in the FD approach are clearly due to the truncation error of the finite-difference scheme in the velocity gradient calculation. The relative magnitudes from the FD approach at different grid resolutions clearly show that the rate of convergence is of second order, which is consistent with our expectation in Eq. (31). Although the magnitudes of these truncation errors in FD appear to be large, as we shall find shortly, they are still about two orders of magnitude smaller than the error magnitude in the strain rate and vorticity in FD at later times. Therefore, the existence of such initial errors should not affect our later observations on the order of accuracy. Therefore, we can safely assume that the L2 norms listed in Tables IV and V for the strain

rate and vorticity at $t^* = 4$ and 8 truly reflect the convergence rate of the errors in both computation approaches.

At $t^* = 4$, except ω_z , the vorticity and strain rate calculated mesoscopically are more accurate than those from the finite-difference approximation, measured by the magnitude of the L2 norm. Both methods exhibit roughly a second-order accuracy for all strain rate and vorticity components but the errors from the mesoscopic approach always have higher convergence rates than their finite-difference counterparts. The magnitudes of the numerical errors in mesoscopic vorticity calculation must be associated with the values of fifth-order equilibrium moments, i.e., ξ_{23} , ξ_{24} , and ξ_{25} , as well as the relevant relaxation parameters s_{7-9} and s_{20-22} , so potentially smaller L2 norm might be achieved with optimized parameter setting. On the other hand, Junk *et al.* [31] showed that

TABLE IV. The L2 norms of strain rate and vorticity errors at ($t^* = 4$) in a decaying Taylor-Green flow.

| n_x | ω_x (FD) | Order | ω_x (ME) | Order | ω_y (FD) | Order | ω_y (ME) | Order | ω_z (FD) | Order | ω_z (ME) | Order |
|---------|-----------------|-------|-----------------|-------|-----------------|-------|-----------------|-------|-----------------|-------|-----------------|-------|
| 64 | 1.494E-1 | (-) | 1.690E-1 | (-) | 1.482E-1 | (-) | 1.563E-1 | (-) | 1.017E-1 | (-) | 2.631E-1 | (-) |
| 128 | 4.935E-2 | 1.598 | 4.282E-2 | 1.981 | 4.754E-2 | 1.640 | 3.851E-2 | 2.021 | 2.910E-2 | 1.805 | 6.877E-2 | 1.936 |
| 256 | 1.276E-2 | 1.951 | 7.430E-3 | 2.527 | 1.216E-2 | 1.967 | 6.416E-3 | 2.585 | 7.336E-3 | 1.988 | 1.253E-2 | 2.456 |
| Overall | | 1.775 | | 2.254 | | 1.803 | | 2.303 | | 1.896 | | 2.196 |
| n_x | s_{xx} (FD) | Order | s_{xx} (ME) | Order | s_{yy} (FD) | Order | s_{yy} (ME) | Order | s_{zz} (FD) | Order | s_{zz} (ME) | Order |
| 64 | 9.933E-2 | (-) | 7.895E-2 | (-) | 9.890E-2 | (-) | 7.926E-2 | (-) | 1.368E-1 | (-) | 9.364E-2 | (-) |
| 128 | 2.689E-2 | 1.885 | 1.847E-2 | 2.096 | 2.731E-2 | 1.856 | 1.837E-2 | 2.109 | 4.512E-2 | 1.601 | 2.365E-2 | 1.985 |
| 256 | 5.948E-3 | 2.177 | 3.829E-3 | 2.270 | 6.024E-3 | 2.181 | 3.484E-3 | 2.398 | 1.178E-2 | 1.937 | 4.363E-3 | 2.438 |
| Overall | | 2.031 | | 2.183 | | 2.018 | | 2.253 | | 1.769 | | 2.211 |
| n_x | s_{xy} (FD) | Order | s_{xy} (ME) | Order | s_{yz} (FD) | Order | s_{yz} (ME) | Order | s_{xz} (FD) | Order | s_{xz} (ME) | Order |
| 64 | 1.553E-1 | (-) | 9.850E-2 | (-) | 1.777E-1 | (-) | 1.217E-1 | (-) | 1.783E-1 | (-) | 1.269E-1 | (-) |
| 128 | 4.682E-2 | 1.730 | 3.114E-2 | 1.661 | 6.070E-2 | 1.550 | 3.058E-2 | 1.993 | 5.977E-2 | 1.577 | 2.933E-2 | 2.113 |
| 256 | 1.226E-2 | 1.933 | 6.771E-3 | 2.202 | 1.618E-2 | 1.908 | 6.644E-3 | 2.202 | 1.570E-2 | 1.928 | 6.725E-3 | 2.125 |
| overall | | 1.831 | | 1.931 | | 1.729 | | 2.097 | | 1.752 | | 2.119 |

TABLE V. The L2 norms of strain rate and vorticity errors at ($t^* = 8$) in a decaying Taylor-Green flow.

| n_x | ω_x (FD) | Order | ω_x (ME) | Order | ω_y (FD) | Order | ω_y (ME) | Order | ω_z (FD) | Order | ω_z (ME) | Order |
|---------|-----------------|-------|-----------------|-------|-----------------|-------|-----------------|-------|-----------------|-------|-----------------|-------|
| 64 | 2.570E-1 | (-) | 4.736E-1 | (-) | 2.546E-1 | (-) | 3.161E-1 | (-) | 2.700E-1 | (-) | 8.547E-1 | (-) |
| 128 | 7.615E-2 | 1.755 | 1.533E-1 | 1.627 | 7.637E-2 | 1.737 | 7.780E-2 | 2.022 | 9.488E-2 | 1.509 | 2.429E-1 | 1.815 |
| 256 | 1.843E-2 | 2.047 | 2.965E-2 | 2.370 | 1.987E-2 | 1.942 | 1.681E-2 | 2.210 | 2.388E-2 | 1.990 | 4.809E-2 | 2.337 |
| Overall | | | | | | | | | | | | 2.076 |
| n_x | s_{xx} (FD) | Order | s_{xx} (ME) | Order | s_{yy} (FD) | Order | s_{yy} (ME) | Order | s_{zz} (FD) | Order | s_{zz} (ME) | Order |
| 64 | 2.420E-1 | (-) | 2.771E-1 | (-) | 2.362E-1 | (-) | 2.589E-1 | (-) | 2.404E-1 | (-) | 2.393E-1 | (-) |
| 128 | 7.702E-2 | 1.652 | 9.185E-2 | 1.593 | 7.360E-2 | 1.682 | 8.678E-2 | 1.577 | 6.302E-2 | 1.932 | 7.065E-2 | 1.760 |
| 256 | 1.903E-2 | 2.017 | 2.218E-2 | 2.050 | 1.660E-2 | 2.148 | 1.961E-2 | 2.146 | 1.547E-2 | 2.026 | 1.700E-2 | 2.055 |
| overall | | | | | | | | | | | | 1.908 |
| n_x | s_{xy} (FD) | Order | s_{xy} (ME) | Order | s_{yz} (FD) | Order | s_{yz} (ME) | Order | s_{xz} (FD) | Order | s_{xz} (ME) | Order |
| 64 | 2.854E-1 | (-) | 4.110E-1 | (-) | 2.720E-1 | (-) | 2.650E-1 | (-) | 2.715E-1 | (-) | 3.479E-1 | (-) |
| 128 | 1.001E-1 | 1.511 | 1.487E-1 | 1.467 | 8.326E-2 | 1.708 | 7.774E-2 | 1.769 | 8.605E-2 | 1.658 | 1.188E-1 | 1.550 |
| 256 | 2.635E-2 | 1.926 | 3.563E-2 | 2.061 | 2.040E-2 | 2.029 | 1.735E-2 | 2.164 | 2.254E-2 | 1.933 | 3.053E-2 | 1.960 |
| overall | | | | | | | | | | | | 1.755 |

the velocity gradients calculated by a second-order finite-difference scheme could maintain second-order accuracy in pure periodic problems. This is because the leading-order velocity error in LBM scales with h^3 instead of h^2 , which can be easily seen via the asymptotic expansion. For more general problems, e.g., flows with solid boundaries, the above statement breaks down and the finite-difference method is only capable of providing vorticity calculation of the first-order accuracy [31].

At the later time $t^* = 8$, for most strain rate and vorticity components, the results calculated through finite-difference approximation have error magnitudes comparable to or smaller than those from moment equations. This indicates that in the present simulation, the computation of conserved moments (i.e., the velocity field) is much more accurate than those of nonconserved moments, from which the vorticity components are obtained. Again, in general, we observe a second-order accuracy for both ME and FD approaches. While for vorticity components, the mesoscopic method has higher convergence rates for the numerical error than the finite difference method, the convergence rates for the strain rate components in the two approaches are comparable.

B. The lid-driven cavity flow

The present model and its mesoscopic vorticity calculation feature are further examined by a 3D lid-driven cavity flow.

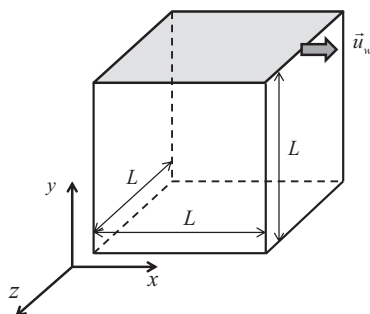


FIG. 7. Sketch of the 3D lid-driven cavity flow.

The flow setting is sketched in Fig. 7, where the fluid at rest initially inside a cubic box with length L is driven by the top lid moving with a constant velocity $\vec{u} = (u_w, 0, 0)$. The other five walls are maintained at zero velocity. The Reynolds number $Re = u_w L / \nu$ is set to 100 and the shear and bulk viscosity are fixed at $\nu = 0.02$ and $\nu^V = 0.0370$. The grid resolution has been adopted as $n_x = n_y = n_z = 256$. The coefficients of high-order equilibrium moments and relaxation parameters are the same as those listed in Table II. The fluid boundary nodes are arranged half lattice spacing from all walls so the accurate midlink bounce back can naturally be applied to represent the no-slip boundary condition.

When the flow reaches the steady state, the vorticity component ω_x at $i = n_x/2$ plane, ω_y at $j = n_y/2$ and ω_z at $k = n_z/2$, are shown in Fig. 8. Here we only qualitatively examine if the present model still ensures correct mesoscopic vorticity calculation with the presence of solid boundaries. Clearly, Fig. 8 shows that the mesoscopically calculated vorticity results are almost identical to those calculated via the FD approximation, except the small region near the singularity edges [see the top corners of Fig. 8(b)]. The mesoscopic vorticity calculation is contaminated more by the noises generated from the singularities than the finite difference approximation. This is again because the large velocity gradients in this region break the quasiequilibrium assumption of LBM, which results in a rather fluctuating off-equilibrium distribution.

C. A uniform flow passing a fixed sphere

Finally, we test the mesoscopic vorticity calculation in the present model for a flow with curved boundary: a uniform flow passing a fixed sphere with a particle Reynolds number $Re_p = UD/\nu = 50$ and 100. As illustrated in Fig. 9, a uniform stream $\mathbf{u} = (U, 0, 0)$ from the inlet passes a fixed sphere with a diameter of $D = 20$ and centered at $(5D, 5D, 5D)$. The computational domain has a size of $20D \times 10D \times 10D$. The stress-free boundary condition is applied to the four side boundaries, which is realized by mirror reflection. For the inlet and outlet, we use the boundary schemes by Lou *et al.* [35].

Our focus here is to test the performance of mesoscopic vorticity calculation in the presence of a curved boundary.

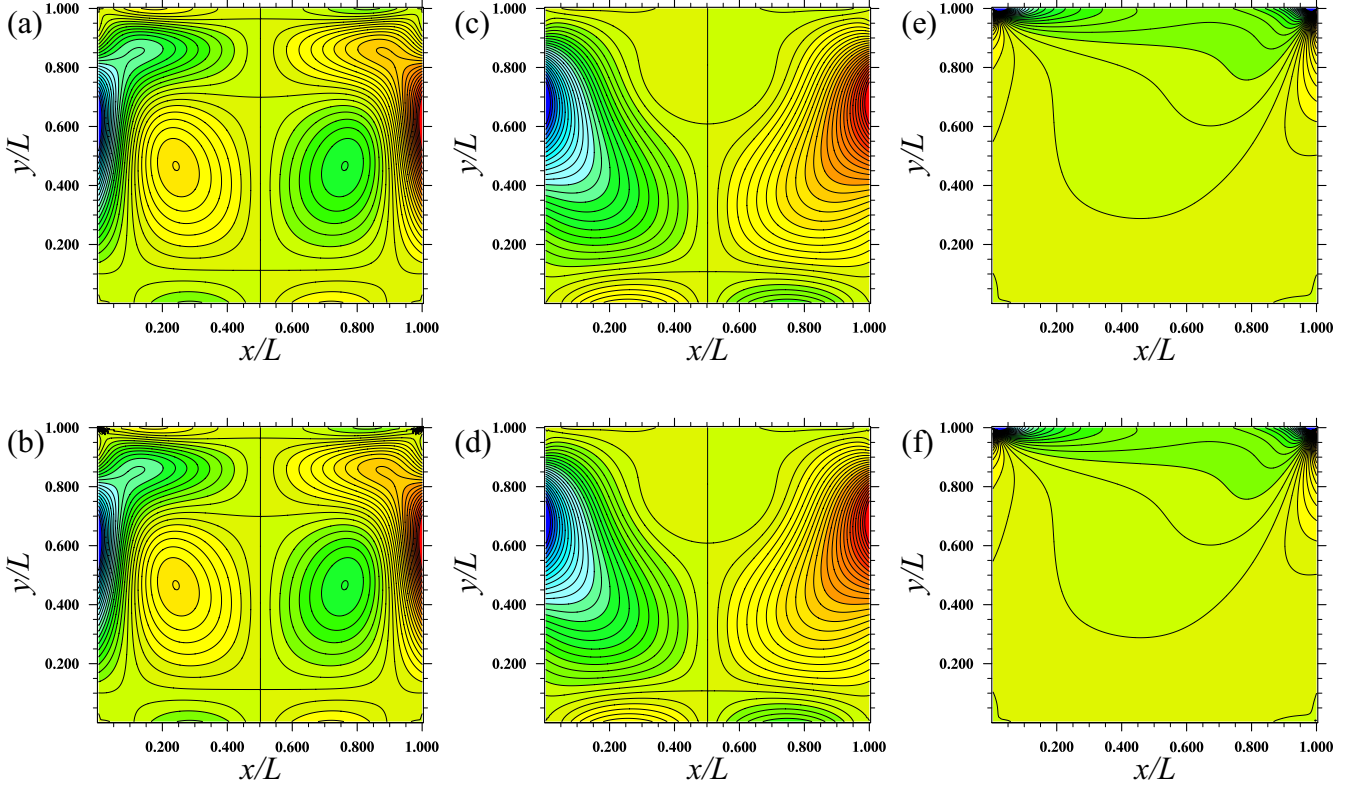


FIG. 8. Contours of vorticity in a lid-driven cavity flow: (a) FD ω_x at $n_x/2$ plane; (b) ME, same as (a); (c) FD, ω_y at $n_y/2$ plane; (d) ME, same as (c); (e) FD, ω_z at $n_z/2$ plane; (f) ME, same as (e).

Different from the previous two cases, here we define $\zeta_{23} = 1.0$, $\zeta_{24} = 1.25$, and $\zeta_{25} = 1.5$, and keep the other coefficients of high-order equilibrium moments and their relaxation parameters identical with those adopted in Table II. At the steady state, vorticity contours in a cut across the particle center are shown in Fig. 10. For completeness, here we also show the corresponding vorticity contours in parallel from the regular MRT model (from finite-difference approximation) to assess the impact of modified high-order equilibrium on the accuracy of the LB model.

As clearly indicated by Fig. 10, the modification of high-order equilibrium moments does not affect the accuracy of LBM, as the vorticity contours from regular MRT model and the present model, both from finite-difference approximation are visually identical with each other. Again, the mesoscopically calculated vorticity contours contain more fluctuations around the stagnation point. This fluctuations can be reduced by either choosing finer grid resolution or optimizing the relevant coefficients on the vorticity calculation.

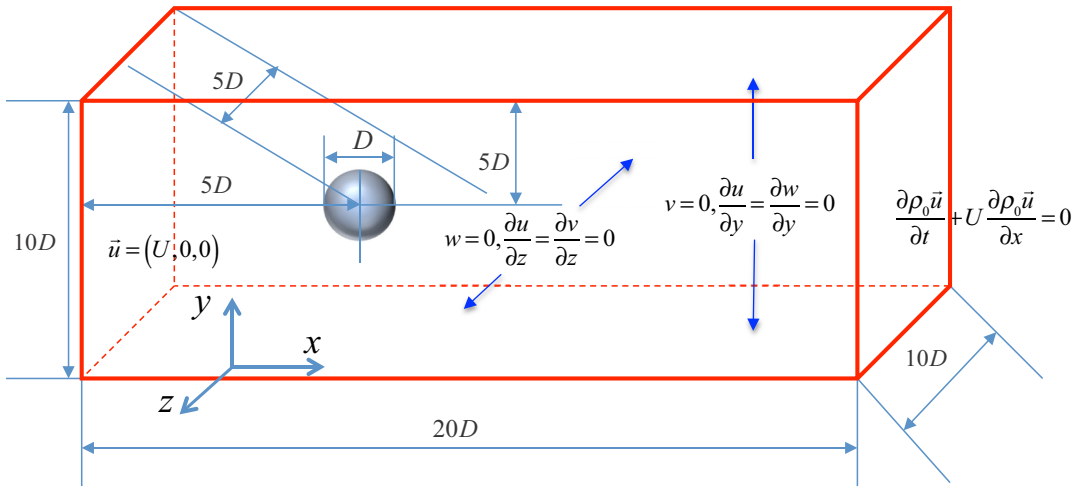


FIG. 9. Sketch of a uniform flow passing a fixed sphere.

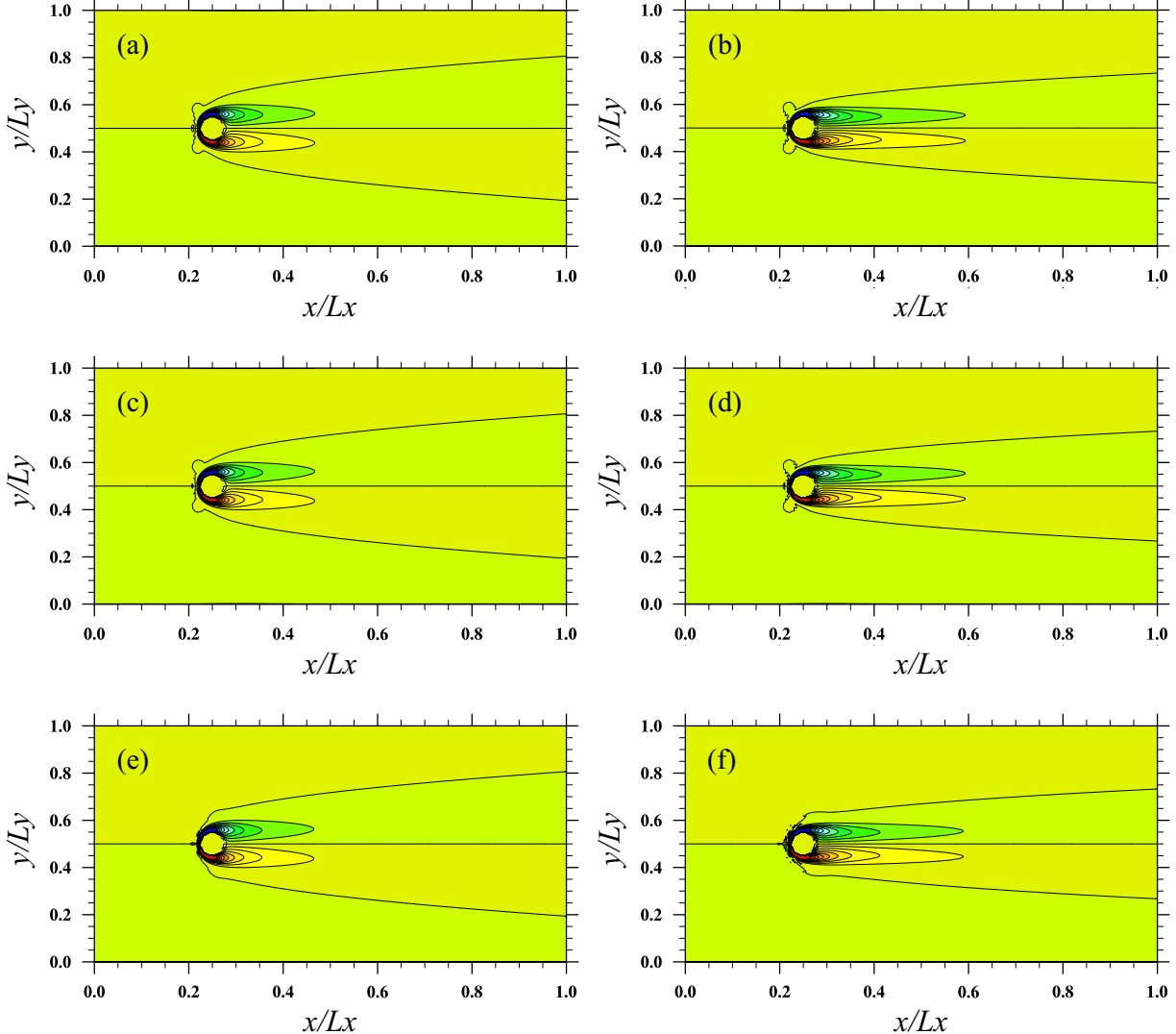


FIG. 10. Vorticity contours in a plane cutting across the sphere center for a uniform flow passing a sphere: (a) standard MRT $Re_p = 50$; (b) standard MRT $Re_p = 100$; (c) present MRT, $Re_p = 50$, with finite-difference approximation; (d) present MRT $Re_p = 100$, with finite-difference approximation; (e) present MRT, $Re_p = 50$, with moment equations; and (f) present MRT $Re_p = 100$, with moment equations.

V. SUMMARY

In this paper, we proposed a D3Q27 MRT LB model in order to realize mesoscopic vorticity calculation. The mesoscopic vorticity calculation, compared with the finite-difference approximation, has several advantages. First, it requires no additional data communication when the parallel computation is involved. Second, it does not require special treatments near complex geometric boundaries. Most importantly, same as the strain rate computation from the nonequilibrium moments, the mesoscopic computation of vorticity is expected to possess a second-order accuracy.

Through a detailed Chapman-Enskog analysis coupled with the concept of inverse design, we identify all the necessary constraints required by the N-S equations. More importantly, we expose all the available degrees of freedom in the model that can be utilized to achieve mesoscopic vorticity calculation. We have demonstrated that, with 27 lattice velocities in the D3Q27 model, all the velocity and pressure gradients can be directly computed from the nonequilibrium moments

when the lattice Boltzmann model is properly designed. We argue that at the hydrodynamic level, the equilibrium of the present MRT LB model does not need to follow the standard, overconstrained LBGK equilibrium. Specifically, we have found that a proper prescription of anisotropy in the fifth-order equilibrium moment can lead to appearance of the three vorticity components in the contracted fourth-order nonequilibrium moment. The same design cannot be achieved with D3Q15 and D3Q19 lattice, since the desired fifth-order moments are unavailable in those models. An asymptotic analysis shows that the mesoscopic vorticity calculation in our model is of second-order accuracy.

The resulting LB model has been validated by simulations of a decaying three-dimensional Taylor-Green vortex flow at $Re_0 = 600\pi$. The simulation results show that the modifications of irrelevant moments introduced in this paper has no adverse impact on the physical accuracy and only a slight negative effect on the numerical stability when compared to the standard LBM models without the capability of mesoscopic

vorticity calculation. The strain rate and vorticity calculated mesoscopically from the nonequilibrium moments are compared against the results from the pseudospectral method. The second-order accuracy of the mesoscopic vorticity calculation is confirmed. Furthermore, we briefly tested the present model in the simulations of a three-dimensional lid-driven cavity flow and a uniform flow passing a sphere. These tests support the accuracy and robustness of our model and its mesoscopic vorticity calculation in the cases when solid boundaries are present.

ACKNOWLEDGMENTS

This work has been supported by the U.S. National Science Foundation (NSF) under Grants No. CBET-1706130, No. CNS1513031, No. CBET-1235974, and No. AGS-1139743 and by Air Force Office of Scientific Research under Grant No. FA9550-13-1-0213. L.P.W. also acknowledges support from the Ministry of Education of P.R. China and Huazhong University of Science and Technology through Chang Jiang

Scholar Visiting Professorship. Computing resources are provided by National Center for Atmospheric Research through Grants No. CISL-P35751014 and No. CISL-UDEL0001 and by University of Delaware through NSF Grant No. CRI 0958512. We thank Dr. Alexander Wagner and an anonymous reviewer for their helpful comments which led to a significantly improved presentation of this paper.

APPENDIX: A TOP-DOWN INTERPRETATION OF THE MODEL DESIGN

In this Appendix, we provide an alternative interpretation of our model design in terms of equilibrium distribution functions. Let us divide the 27 equilibrium distribution functions into four groups: the 0-speed group $\alpha = 0$; the 1-speed group $\alpha = 1, 2, \dots, 6$; the $\sqrt{2}$ -speed group $\alpha = 7, 8, \dots, 18$; the $\sqrt{3}$ -speed group $\alpha = 19, 20, \dots, 26$. Instead of following the LBGK equilibrium distribution in Eq. (16), the equilibrium distribution in our model is modified as

$$f_{\alpha}^{(\text{eq})} = w_{\alpha}\delta\rho + \rho_0 w_{\alpha} \left[\frac{b(\alpha,1)e_{\alpha 1}u_1 + b(\alpha,2)e_{\alpha 2}u_2 + b(\alpha,3)e_{\alpha 3}u_3}{c_s^2} + \frac{(e_{\alpha i}u_i)^2}{2c_s^4} + \frac{u_iu_i}{2c_s^2} \right], \quad (\text{A1})$$

where the first term inside the square brackets for the 1-speed group, $\sqrt{2}$ -speed group, and $\sqrt{3}$ -speed group are explicitly written as

$$f_{\alpha}^{(1,\text{eq})} = \frac{\rho_0 w_{\alpha}}{c_s^2} \left(\frac{3 + \zeta'_1}{4} u_1 e_{\alpha 1} + \frac{3 + \zeta'_2}{4} u_2 e_{\alpha 2} + \frac{3 + \zeta'_3}{4} u_3 e_{\alpha 3} \right), \quad \text{for } \alpha = 1, 2, \dots, 6. \quad (\text{A2})$$

$$f_{\alpha}^{(1,\text{eq})} = \frac{\rho_0 w_{\alpha}}{c_s^2} \left(\frac{3 - \zeta'_1}{2} u_1 e_{\alpha 1} + \frac{3 - \zeta'_2}{2} u_2 e_{\alpha 2} + \frac{3 - \zeta'_3}{2} u_3 e_{\alpha 3} \right), \quad \text{for } \alpha = 7, 8, \dots, 18. \quad (\text{A3})$$

$$f_{\alpha}^{(1,\text{eq})} = \frac{\rho_0 w_{\alpha}}{c_s^2} (\zeta'_1 u_1 e_{\alpha 1} + \zeta'_2 u_2 e_{\alpha 2} + \zeta'_3 u_3 e_{\alpha 3}), \quad \text{for } \alpha = 19, 20, \dots, 26. \quad (\text{A4})$$

Namely, the newly introduced adjustable parameters $b(\alpha,i), i = 1, 2, 3$ are only functions of three scalar parameters ζ'_1, ζ'_2 , and ζ'_3 . The standard equilibrium is recovered when $\zeta'_1 = \zeta'_2 = \zeta'_3 = 1$. The above specific forms are derived directly from the results of the bottom-up derivation presented in Sec. III. Note that the three coefficients have no impact on all the even moments of $f_{\alpha}^{(\text{eq})}$, provided that $f_{\alpha}^{(1,\text{eq})}(\mathbf{e}_{\alpha}) = -f_{\alpha}^{(1,\text{eq})}(\mathbf{e}_{\bar{\alpha}})$ if $\mathbf{e}_{\bar{\alpha}} = -\mathbf{e}_{\alpha}$. This symmetry property is preserved here. Here and later, the weighting coefficients w_{α} remain identical to the values in the standard LBGK equilibrium distributions, namely 2/27, 1/54, 1/216, for the 1-speed, $\sqrt{2}$ -speed, and $\sqrt{3}$ -speed groups, respectively. No change is made to the 0-speed group as it makes a null contribution to all moments except density. The essence of our model design is to introduce three adjustable coefficients ζ'_1, ζ'_2 , and ζ'_3 into the equilibrium distribution, in a special manner, such that the first- and third-order moments of $f_{\alpha}^{(\text{eq})}$ are unchanged, but the fifth-order moments of $f_{\alpha}^{(\text{eq})}$ are altered.

Now let us examine how the above goal is accomplished. In our model, the partial contributions of the 1-speed, $\sqrt{2}$ -speed, and $\sqrt{3}$ -speed groups to first-order moments are, respectively,

$$\sum_{\alpha=1}^6 f_{\alpha}^{(1,\text{eq})} e_{\alpha,i} = \frac{4}{9} \rho_0 \frac{3 + \zeta'_i}{4} u_i, \quad (\text{A5})$$

$$\sum_{\alpha=7}^{18} f_{\alpha}^{(1,\text{eq})} e_{\alpha,i} = \frac{4}{9} \rho_0 \frac{3 - \zeta'_i}{2} u_i, \quad (\text{A6})$$

$$\sum_{\alpha=19}^{26} f_{\alpha}^{(1,\text{eq})} e_{\alpha,i} = \frac{1}{9} \rho_0 \zeta'_i u_i, \quad (\text{A7})$$

where no summation is implied to the right-hand side for the repeated indices. Clearly, this specific design renders the summation of the three partial contributions to the first-order moment unchanged, namely

$$\sum_{\alpha=1}^{26} f_{\alpha}^{(1,\text{eq})} e_{\alpha,i} = \rho_0 u_i, \quad (\text{A8})$$

which is identical to the first-order equilibrium moment of the standard LBGK model. Similarly, for the third-order moment, the partial contributions of the 1-speed, $\sqrt{2}$ -speed, and $\sqrt{3}$ -speed groups are, respectively,

$$\sum_{\alpha=1}^6 f_{\alpha}^{(1,\text{eq})} e_{\alpha,i} e_{\alpha,j} e_{\alpha,k} = \frac{4}{27} \rho_0 \left(\frac{3 + \zeta'_i}{4} u_i \delta_{jk} + \frac{3 + \zeta'_j}{4} u_j \delta_{ik} + \frac{3 + \zeta'_k}{4} u_k \delta_{ij} \right), \quad (\text{A9})$$

$$\sum_{\alpha=7}^{18} f_{\alpha}^{(1,\text{eq})} e_{\alpha,i} e_{\alpha,j} e_{\alpha,k} = \frac{4}{27} \rho_0 \left(\frac{3 - \zeta'_i}{2} u_i \delta_{jk} + \frac{3 - \zeta'_j}{2} u_j \delta_{ik} + \frac{3 - \zeta'_k}{2} u_k \delta_{ij} \right), \quad (\text{A10})$$

$$\sum_{\alpha=19}^{26} f_{\alpha}^{(1,\text{eq})} e_{\alpha,i} e_{\alpha,j} e_{\alpha,k} = \frac{1}{27} \rho_0 (\zeta'_i u_i \delta_{jk} + \zeta'_j u_j \delta_{ik} + \zeta'_k u_k \delta_{ij}). \quad (\text{A11})$$

Therefore, the summation of three partial contributions are

$$\sum_{\alpha=1}^{26} f_{\alpha}^{(1,\text{eq})} e_{\alpha,i} e_{\alpha,j} e_{\alpha,k} = \frac{1}{3} \rho_0 (u_i \delta_{jk} + u_j \delta_{ik} + u_k \delta_{ij}), \quad (\text{A12})$$

which is again independent of ζ'_i and has an isotropic form identical to that in the standard LBGK model. Finally, the partial contributions to the three nontrivial components of the fifth-order equilibrium moment are

$$\sum_{\alpha=1}^6 f_{\alpha}^{(1,\text{eq})} \| \mathbf{e}_{\alpha} \|^4 e_{\alpha,i} = \frac{4}{9} \rho_0 \frac{3 + \zeta'_i}{4} u_i, \quad (\text{A13})$$

$$\sum_{\alpha=7}^{18} f_{\alpha}^{(1,\text{eq})} \| \mathbf{e}_{\alpha} \|^4 e_{\alpha,i} = \frac{16}{9} \rho_0 \frac{3 - \zeta'_i}{2} u_i, \quad (\text{A14})$$

$$\sum_{\alpha=19}^{26} f_{\alpha}^{(1,\text{eq})} \| \mathbf{e}_{\alpha} \|^4 e_{\alpha,i} = \rho_0 \zeta'_i u_i. \quad (\text{A15})$$

Note here we focus on those components of the fifth-order equilibrium moment that are actually used in our model (see Secs. II A and III), instead of the general form, in order to make a concise deliberation of the fifth-order equilibrium moment. Different from the first and third-order equilibrium moments, the summation of the three partial contributions yields

$$\sum_{\alpha=1}^{26} f_{\alpha}^{(1,\text{eq})} \| \mathbf{e}_{\alpha} \|^4 e_{\alpha,i} = 3 \rho_0 u_i + \frac{2}{9} \zeta'_i \rho_0 u_i, \quad (\text{A16})$$

which is no longer isotropic as ζ'_i are set differently for different spatial directions. The unaltered first- and third-order equilibrium moments guarantee that the N-S equations are unaltered, while the modified fifth-order equilibrium moment introduces anisotropy to allow the three vorticity components to be recovered through the nondiagonal, contracted fourth-order nonequilibrium moment $R_{ij} \equiv \sum f_{\alpha}^{(\text{neq})} | \mathbf{e}_{\alpha} |^2 e_{\alpha,i} e_{\alpha,j}$. Namely, while R_{ij} remains symmetric, its nondiagonal components can be expressed, based on the Chapman-Enskog expansion, as

$$R_{yz} = R_{zy} \approx -\rho_0 \tau \delta t \left[\frac{2}{3} + \frac{\zeta'_2 + \zeta'_3}{18} \right] (\partial_y w + \partial_z v) + \rho_0 \tau \delta t \frac{(\zeta'_2 - \zeta'_3)}{18} \omega_x, \quad (\text{A17})$$

$$R_{xz} = R_{zx} \approx -\rho_0 \tau \delta t \left[\frac{2}{3} + \frac{\zeta'_3 + \zeta'_1}{18} \right] (\partial_z u + \partial_x w) + \rho_0 \tau \delta t \frac{(\zeta'_3 - \zeta'_1)}{18} \omega_y, \quad (\text{A18})$$

$$R_{xy} = R_{yx} \approx -\rho_0 \tau \delta t \left[\frac{2}{3} + \frac{\zeta'_1 + \zeta'_2}{18} \right] (\partial_x v + \partial_y u) + \rho_0 \tau \delta t \frac{(\zeta'_1 - \zeta'_2)}{18} \omega_z, \quad (\text{A19})$$

which contain the three vorticity components explicitly when $\zeta'_1 \neq \zeta'_2 \neq \zeta'_3$. These are also fully consistent with the more general results shown in Eqs. (20a) to (20c).

- [1] C. K. Aidun and J. R. Clausen, Lattice-Boltzmann method for complex flows, *Annu. Rev. Fluid Mech.* **42**, 439 (2010).
- [2] N. Geneva, C. Peng, X. Li, and L.-P. Wang, A scalable interface-resolved simulation of particle-laden flow using the lattice Boltzmann method, *Parallel Comput.* **67**, 20 (2017).
- [3] P. J. Dellar, Bulk and shear viscosities in lattice Boltzmann equations, *Phys. Rev. E* **64**, 031203 (2001).
- [4] M. L. Minion and D. L. Brown, Performance of under-resolved two-dimensional incompressible flow simulations, II, *J. Comput. Phys.* **138**, 734 (1997).
- [5] H. Gao, H. Li, and L.-P. Wang, Lattice Boltzmann simulation of turbulent flow laden with finite-size particles, *Comput. Math. Appl.* **65**, 194 (2013).
- [6] F. Lucci, A. Ferrante, and S. Elghobashi, Modulation of isotropic turbulence by particles of Taylor length-scale size, *J. Fluid Mech.* **650**, 5 (2010).
- [7] Y. Peng, W. Liao, L.-S. Luo, and L.-P. Wang, Comparison of the lattice Boltzmann and pseudo-spectral methods for decaying turbulence: Low-order statistics, *Comput. Fluids* **39**, 568 (2010).
- [8] T. Krüger, F. Varnik, and D. Raabe, Second-order convergence of the deviatoric stress tensor in the standard Bhatnagar-Gross-Krook lattice Boltzmann method, *Phys. Rev. E* **82**, 025701 (2010).
- [9] W.-A. Yong, L.-S. Luo, Accuracy of the viscous stress in the lattice Boltzmann equation with simple boundary conditions, *Phys. Rev. E* **86**, 065701 (2012).
- [10] C. Peng, Z. Guo, and L.-P. Wang, A lattice-BGK model for the Navier-Stokes equations based on a rectangular grid, *Comput. Math. Appl.*, doi: [10.1016/j.camwa.2016.05.007](https://doi.org/10.1016/j.camwa.2016.05.007) (2016).
- [11] J. Latt, B. Chopard, O. Malaspinas, M. Deville, and A. Michler, Straight velocity boundaries in the lattice Boltzmann method, *Phys. Rev. E* **77**, 056703 (2008).
- [12] L.-S. Luo, W. Liao, X. Chen, Y. Peng, W. Zhang, Numerics of the lattice Boltzmann method: Effects of collision models on the lattice Boltzmann simulations, *Phys. Rev. E* **83**, 056710 (2011).
- [13] S. K. Robinson, Coherent motions in the turbulent boundary layer, *Annu. Rev. Fluid Mech.* **23**, 601 (1991).
- [14] M. S. Chong, A. E. Perry, and B. J. Cantwell, A general classification of three-dimensional flow fields, *Phys. Fluids A* **2**, 765 (1990).
- [15] J. Jeong and F. Hussain, On the identification of a vortex, *J. Fluid Mech.* **285**, 69 (1995).
- [16] J. Zhou, R. J. Adrian, S. Balachandar, and T. Kendall, Mechanisms for generating coherent packets of hairpin vortices in channel flow, *J. Fluid Mech.* **387**, 353 (1999).
- [17] P. Lallemand and L.-S. Luo, Theory of the lattice Boltzmann method: Dispersion, dissipation, isotropy, galilean invariance, and stability, *Phys. Rev. E* **61**, 6546 (2000).
- [18] X. Shan, X.-F. Yuan, and H. Chen, Kinetic theory representation of hydrodynamics: a way beyond the Navier-Stokes equation, *J. Fluid Mech.* **550**, 413 (2006).
- [19] H. Min, C. Peng, Z. Guo, and L.-P. Wang, An inverse design analysis of mesoscopic implementation of non-uniform forcing in MRT lattice Boltzmann models, *Comput. Math. Appl.*, doi: [10.1016/j.camwa.2016.04.040](https://doi.org/10.1016/j.camwa.2016.04.040) (2016).
- [20] D. d'Humières, Multiple-relaxation-time lattice Boltzmann models in three dimensions, *Philos. Trans. Roy. Soc. Lond. A* **360**, 437 (2002).
- [21] L.-P. Wang, H. Min, C. Peng, N. Geneva, and Z. Guo, A lattice-Boltzmann scheme of the Navier-Stokes equation on a three-dimensional cuboid lattice, *Comput. Math. Appl.*, doi: [10.1016/j.camwa.2016.06.017](https://doi.org/10.1016/j.camwa.2016.06.017) (2016).
- [22] G. B. Arfken, H. J. Weber, and F. E. Harris, *Mathematical Methods for Physicists: A Comprehensive Guide* (Academic Press, San Diego, CA, 2011).
- [23] Y. Zong, C. Peng, Z. Guo, and L.-P. Wang, Designing correct fluid hydrodynamics on a rectangular grid using MRT lattice Boltzmann approach, *Comput. Math. Appl.* **72**, 288 (2016).
- [24] X. He and L.-S. Luo, Lattice Boltzmann model for the incompressible Navier-Stokes equation, *J. Stat. Phys.* **88**, 927 (1997).
- [25] R. Du, B. Shi, and X. Chen, Multi-relaxation-time lattice Boltzmann model for incompressible flow, *Phys. Lett. A* **359**, 564 (2006).
- [26] D. Rui and B. Shi, Incompressible multi-relaxation-time lattice Boltzmann model in 3D space, *J. Hydromech. Ser. B* **22**, 782 (2010).
- [27] K. Suga, Y. Kuwata, K. Takashima, and R. Chikasue, A D3Q27 multiple-relaxation-time lattice Boltzmann method for turbulent flows, *Comput. Math. Appl.* **69**, 518 (2015).
- [28] C. Peng, H. Min, Z. Guo, and L.-P. Wang, A hydrodynamically-consistent MRT lattice Boltzmann model on a 2D rectangular grid, *J. Computat. Phys.* **326**, 893 (2016).
- [29] W.-A. Yong, W. Zhao, L.-S. Luo, Theory of the lattice Boltzmann method: Derivation of macroscopic equations via the Maxwell iteration, *Phys. Rev. E* **93**, 033310 (2016).
- [30] W. Zhao and W.-A. Yong, Single-node second-order boundary schemes for the lattice Boltzmann method, *J. Comput. Phys.* **329**, 1 (2017).
- [31] M. Junk, A. Klar, and L.-S. Luo, Asymptotic analysis of the lattice Boltzmann equation, *J. Comput. Phys.* **210**, 676 (2005).
- [32] G. Taylor and A. Green, Mechanism of the production of small eddies from large ones, *Proc. R. Soc. Lond. A* **158**, 499 (1937).
- [33] R. Mei, L.-S. Luo, P. Lallemand, and D. d'Humières, Consistent initial conditions for lattice Boltzmann simulations, *Comput. Fluids* **35**, 855 (2006).
- [34] R. Ramadugu, S. P. Thampi, R. Adhikari, S. Succi, and S. Ansumali, Lattice differential operators for computational physics, *Europhys. Lett.* **101**, 50006 (2013).
- [35] Q. Lou, Z. Guo, and B. Shi, Evaluation of outflow boundary conditions for two-phase lattice Boltzmann equation, *Phys. Rev. E* **87**, 063301 (2013).